

# THE ROLE OF STAR FORMATION AND AN AGN IN DUST HEATING OF $z = 0.3$ – $2.8$ GALAXIES. I. EVOLUTION WITH REDSHIFT AND LUMINOSITY

ALLISON KIRKPATRICK<sup>1</sup>, ALEXANDRA POPE<sup>1</sup>, ANNA SAJINA<sup>2</sup>, ERIC ROEBUCK<sup>2</sup>, LIN YAN<sup>3</sup>,  
LEE ARMUS<sup>4</sup>, TANIO DÍAZ-SANTOS<sup>5</sup>, AND SABRINA STIERWALT<sup>6</sup>

<sup>1</sup> Department of Astronomy, University of Massachusetts, Amherst, MA 01002, USA; [kirkpatr@astro.umass.edu](mailto:kirkpatr@astro.umass.edu)

<sup>2</sup> Department of Physics & Astronomy, Tufts University, Medford, MA 02155, USA

<sup>3</sup> Infrared Processing and Analysis Center, California Institute of Technology, Pasadena, CA 91125, USA

<sup>4</sup> Spitzer Science Center, California Institute of Technology, Pasadena, CA 91125, USA

<sup>5</sup> Núcleo de Astronomía de la Facultad de Ingeniería, Universidad Diego Portales, Av. Ejército Libertador 441, Santiago, Chile

<sup>6</sup> Department of Astronomy, University of Virginia, Charlottesville, VA 22904, USA

Received 2015 July 13; accepted 2015 October 8; published 2015 November 10

## ABSTRACT

We characterize infrared spectral energy distributions of 343 (ultra)luminous infrared galaxies from  $z = 0.3$ – $2.8$ . We diagnose the presence of an active galactic nucleus (AGN) by decomposing individual *Spitzer* mid-IR spectroscopy into emission from star formation and an AGN-powered continuum; we classify sources as star-forming galaxies (SFGs), AGNs, or composites. Composites comprise 30% of our sample and are prevalent at faint and bright  $S_{24}$ , making them an important source of IR AGN emission. We combine spectroscopy with multiwavelength photometry, including *Herschel* imaging, to create three libraries of publicly available templates (2–1000  $\mu\text{m}$ ). We fit the far-IR emission using a two-temperature modified blackbody to measure cold and warm dust temperatures ( $T_c$  and  $T_w$ ). We find that  $T_c$  does not depend on mid-IR classification, while  $T_w$  shows a notable increase as the AGN grows more luminous. We measure a quadratic relationship between mid-IR AGN emission and total AGN contribution to  $L_{\text{IR}}$ . AGNs, composites, and SFGs separate in  $S_8/S_{3.6}$  and  $S_{250}/S_{24}$ , providing a useful diagnostic for estimating relative amounts of these sources. We estimate that  $>40\%$  of IR-selected samples host an AGN, even at faint selection thresholds ( $S_{24} > 100 \mu\text{Jy}$ ). Our decomposition technique and color diagnostics are relevant given upcoming observations with the *James Webb Space Telescope*.

**Key words:** galaxies: active – galaxies: evolution – galaxies: ISM – galaxies: star formation – infrared: galaxies

## 1. INTRODUCTION

Internally, galaxy evolution is driven by ongoing star formation and an active galactic nucleus (AGN), and these two processes often occur simultaneously in massive galaxies. Evolved galaxies formed most of their stellar and black hole mass in the era  $z \sim 1$ – $3$ , making high-redshift sources invaluable for disentangling how the growth of an AGN impacts the interstellar medium (ISM) of an actively star-forming galaxy (SFG; Madau & Dickinson 2014 and references therein). The majority of the black hole activity in the early universe is occurring behind dust screens, as evidenced by the largely unresolved cosmic X-ray background at energies  $>6$  keV (Hickox & Markevitch 2007). In addition, the bulk of the star formation during this period is occurring in luminous ( $L_{\text{IR}} > 10^{11} L_{\odot}$ ) and ultraluminous infrared galaxies ( $L_{\text{IR}} > 10^{12} L_{\odot}$ ), known as (U)LIRGs (e.g., Murphy et al. 2011). (U)LIRGs at high redshift form stars at prodigious rates (star formation rate (SFR)  $\geq 10$ – $100 M_{\odot} \text{ yr}^{-1}$ ), and many show signs of concurrent AGN growth (e.g., Sajina et al. 2007; Pope et al. 2008; Coppin et al. 2010; Kirkpatrick et al. 2012), providing an attractive option for studying the simultaneous assembly of black hole and stellar mass.

Since a large fraction of star formation and AGN activity in the early universe is obscured by dust, it is necessary to turn to the infrared spectrum to study these processes. Ubiquitous infrared data from space telescopes have made it possible to identify star-forming and AGN signatures in the dust emission. In the near-IR,  $\text{H}^-$  emission from the older stellar population is visible as a stellar bump, peaking at  $1.6 \mu\text{m}$ . However, if an AGN is present, it can heat the surrounding torus to

$T \gtrsim 1000$  K, causing the dust to radiate into the near-IR and obscure the stellar bump (Donley et al. 2012). The mid-IR spectrum is the most rich for identifying signatures of AGNs and star formation, as it contains dust and gas emission/absorption lines and an underlying continuum. The most prominent dust emission complexes are produced by polycyclic aromatic hydrocarbons (PAHs); PAHs are abundant in galaxies with metallicity close to solar, such as high-redshift (U)LIRGs (Magdis et al. 2012). PAHs are excited by UV and optical photons and are primarily located in star-forming regions; as such, PAHs are good tracers of the rate of star formation in a galaxy (Peeters et al. 2004). Additionally, the mid-IR spectrum may exhibit continuum emission coming from very small dust grains stochastically heated by the interstellar radiation field, or a stronger, steeply rising continuum due to emission from a hot dusty torus enveloping the AGN.

The bulk of IR luminosity is emitted in the far-IR, which comprises warm dust ( $T \sim 60$ – $100$  K) and cold dust ( $T \sim 20$  K) components; the temperatures and relative amounts of each component are an excellent indicator of the dominant power source in a galaxy (Kirkpatrick et al. 2012). The warm and cold dust components arise from different locations in the ISM (Dunne & Eales 2001). The cold dust is located in the diffuse ISM and is emission from large dust grains and the bulk of the dust mass. The warm dust emanates in star-forming regions, or is possibly heated by radiation from an AGN.

Even with the availability of an abundance of infrared data, observations at high redshift are still limited due to either confusion limits of telescopes or long required integration times for faint galaxies. As a result, a common technique is to apply local templates to scant photometry for distant galaxies in

order to extrapolate information about their star formation rates (SFRs),  $L_{\text{IR}}$ , or dust masses. In particular, many authors scale the appropriate Chary & Elbaz (2001) template to a  $24\,\mu\text{m}$  photometric point to estimate  $L_{\text{IR}}$ . However, this technique has been shown to overestimate  $L_{\text{IR}}$  at  $z > 1.5$ , likely due to the changing nature of ULIRGs (e.g., Nordon et al. 2010; Elbaz et al. 2011; Magnelli et al. 2011). The Chary & Elbaz (2001) templates were derived from local galaxies, and local ULIRGs are almost exclusively undergoing a major merger. A major merger of two galaxies triggers a spatially compact burst of star formation and the subsequent growth of the AGN (Sanders & Mirabel 1996). Out to  $z \approx 1.5$ , the SFR and specific SFR ( $\text{sSFR} = \text{SFR}/M_*$ ) increase in disk galaxies as they approach neighbors, and after an interaction, luminous AGN signatures are detectable in the mid-infrared (Hwang et al. 2011; Zamojski et al. 2011). In contrast, at  $z \sim 2$ , a significant fraction of ULIRGs have a disk morphology and lack any merger signatures, likely because the increased gas fractions can sustain the high SFRs without requiring a merger (Elbaz et al. 2011; Kartaltepe et al. 2012).

Assigning low-redshift templates to high-redshift sources correctly presents a serious problem for high-redshift studies, and astronomers have addressed this problem by creating empirical high-redshift templates from stacked spectral energy distributions (SEDs; Elbaz et al. 2011; Kirkpatrick et al. 2012; Sajina et al. 2012; Lee et al. 2013). In particular, Kirkpatrick et al. (2012) and Sajina et al. (2012) use mid-IR spectroscopy to diagnose the presence of an AGN, and then stack photometry and spectroscopy to measure the average IR emission properties of AGNs and SFGs. Using mid-IR spectroscopy to identify AGNs allows the authors to find AGNs that might be missed at other wavelengths due to dust obscuration, and the resulting templates can then be used to assess the presence of an AGN in high-redshift galaxies that have only a few photometric observations (Kirkpatrick et al. 2013; Nelson et al. 2014; Stanley et al. 2015). Kirkpatrick et al. (2012) and Sajina et al. (2012) are limited by the number of galaxies with available mid-IR spectroscopy. Due to sample size, those studies mainly compare the IR properties of SFGs and AGNs, but do not focus on composite sources that have a mixture of both star formation and AGN activity.

In this paper, we extend the work of Kirkpatrick et al. (2012) and Sajina et al. (2012) by combining the individual samples to create a large sample of 343 high-redshift (U)LIRGs. With this combined sample, we are able to probe the effect of a growing AGN on the observed SED by classifying sources as SFGs, AGNs, and composites. We are also able to quantify changes in the dust emission as a function of redshift and  $L_{\text{IR}}$ . We create three libraries of empirical IR SED templates, which we make publicly available. Our sample is *unique* in that all of our sources have mid-IR spectroscopy, allowing us to robustly separate AGNs from SFGs. With our statistically significant sample and template libraries, we investigate how the dust properties, such as temperatures and heating sources, vary as the AGN grows more luminous. In Section 2, we describe our sample and data sets, and in Section 3, we discuss our mid-IR decomposition technique, which allows us to determine the presence/strength of an AGN. In Section 4, we present our three empirical template libraries. In Section 5, we discuss the relationship between AGN signatures in the mid-IR and the total contribution of an AGN to  $L_{\text{IR}}$ . In Section 6, we consider how the dust properties of high-redshift (U)LIRGs, as indicated

**Table 1**  
IRS Sample

PID	# of Sources <sup>a</sup>	References
20629	136	Dasyra et al. (2009)
30431	49 + 15	Fadda et al. (2010)
3748	39	Yan et al. (2007)
20456	22 + 2	Pope et al. (2008), Murphy et al. (2009)
40918	13 + 2	...
20733	10 + 2	...
288	6	Pope et al. (2013)
3216	6	...
20083	6	Lacy et al. (2007)
15	5	Weedman et al. (2006), Martínez-Sansigre et al. (2008)
252	2 + 2	Teplitz et al. (2007)
20081	4	Menéndez-Delmestre et al. (2009)
30419	4	Donley et al. (2010)
20128	4	...
50419	2	...
50305	3	...
30447	2	...
3223	1	Sturm et al. (2006)
531	1	Carilli et al. (2010), Riechers et al. (2014)
20542	1	...
20767	1	...
50324	1	...
50512	1	...
50647	1	...

**Notes.** We list the *Spitzer* Program ID (PID) of our sources, the number of sources from that program, and a reference when available. We stress that we have reduced all data from these programs ourselves and apply our own spectral decomposition in a consistent manner.

<sup>a</sup> A few programs resulted in so-called bonus sources that were not a part of the initial target list. We list the number of bonus sources after the “+” sign.

by our templates, relate to AGN growth and galaxy evolution. Finally, we summarize our findings in Section 7. Throughout this paper, we adopt a standard cosmology with  $H_0 = 70\,\text{km s}^{-1}\,\text{Mpc}^{-1}$ ,  $\Omega_M = 0.3$ , and  $\Omega_\Lambda = 0.7$ .

## 2. SAMPLE AND OBSERVATIONS

### 2.1. Sample Description

We have assembled a multiwavelength data set for a sample of 343 high-redshift ( $z \sim 0.3\text{--}2.8$ ) (U)LIRGs in the Great Observatories Origins Deep Survey North (GOODS-N), Extended *Chandra* Deep Field Survey (ECDFS), and *Spitzer* Extragalactic First Look Survey (xFLS) fields. All sources are selected to have mid-IR spectroscopy from the *Spitzer Space Telescope* Infrared Spectrograph (IRS), necessary to concretely quantify the IR AGN emission in each galaxy. Our sample contains a range of sources from individual observing programs, each with differing selection criteria. However, the overarching selection criterion is that each galaxy must be bright enough at  $24\,\mu\text{m}$  (observed frame) to be detectable in  $<10\,\text{hr}$ . More specific properties of the different fields are outlined below.

The xFLS sample comprises archival sources with IRS spectroscopy (complete sample details can be found in Sajina et al. 2012). The sources were selected to have an observed  $24\,\mu\text{m}$  flux density greater than  $0.9\,\text{mJy}$  and to have an  $R$  magnitude of  $m_{R,\text{Vega}} \geq 20$ . *Spitzer* Program IDs and references are listed in Table 1. The xFLS IRS sample contains just under half of the xFLS sources that meet the above photometric

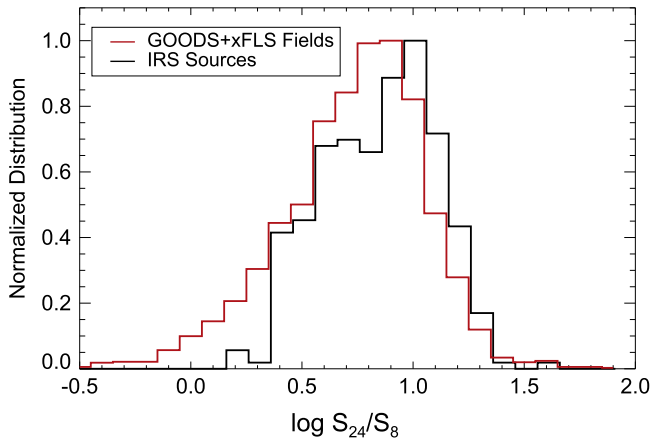


**Figure 1.** Distribution in  $S_{24}/S_8$  (observed) for our IRS sample (black) compared with the full xFLS and GOODS fields (red). We have down-weighted the distribution of xFLS sources (each source is assigned a weight of 0.03) to account for the difference in the sizes of the GOODS and xFLS fields. The IRS sample is representative of the full fields except for very blue sources ( $\log S_{24}/S_8 < 0.1$ ), which are likely undetected in the far-IR.

criteria; however, Sajina et al. (2012) find that the IRS sample has the same  $S_{24}/S_8$  color distribution as the parent sample and is representative of a  $24\ \mu\text{m}$  selected sample ( $>0.9\ \text{mJy}$ ) at  $z \gtrsim 1$ . The  $m_{R,\text{Vega}} > 20$  criterion removes the  $z \sim 0.2$  peak found in the redshift distribution of a purely  $24\ \mu\text{m}$  selected sample.

The GOODS-N and ECDFS samples include all sources in these fields that were observed with *Spitzer* IRS (complete details are in Kirkpatrick et al. 2012). All of these sources were selected at  $24\ \mu\text{m}$  (observed), and 93% of them have  $S_{24} > 100\ \mu\text{Jy}$ . The IRS sources occupy the same regions in  $S_{250}/S_{24}$  and  $S_8/S_{3.6}$  colorspace as the parent MIPS  $24\ \mu\text{m}$  GOODS sample with  $S_{24} > 100\ \mu\text{Jy}$ , and they have a similar redshift distribution as those MIPS sources in GOODS for which we have redshift estimates ( $\sim 750$  sources).

We illustrate the representativeness of the combined sample in Figure 1. We plot the distribution of  $S_{24}/S_8$  for our IRS sources, and we compare with the full distribution of GOODS-N, GOODS-S, and xFLS sources. We are limited by the choice of color due to the different wavelength coverage and depths of the xFLS and GOODS fields. We combine  $S_8$  with  $S_{24}$  as this color traces the relative amount of PAH emission or silicate absorption compared with warm continuum emission, both of which we use to diagnose the presence of an AGN. The xFLS field ( $2.7\ \text{deg}^2$ ) is much larger than the GOODS fields ( $0.09\ \text{deg}^2$ ), so we have weighted the distribution of the xFLS sources by the ratio of the field areas. The distributions are not consistent, which is a natural result of our combining several samples with different selection criteria. However, our IRS sample is generally representative of the GOODS and xFLS fields in the  $S_{24}/S_8$  color, although there is a subset of sources with low  $S_{24}/S_8$  ratios that we are missing. It is important for the reader to bear in mind that for this study we are interested in sources that have mid-IR spectroscopy and PACS or SPIRE photometry. Sources with low  $S_{24}/S_8$  ratios are likely to be very faint at longer wavelengths. This sample is representative of sources that are detected in both the mid-IR and far-IR and may not cover the parameter space of sources fainter than our flux limits in either IR regime.

An additional result of our different  $S_{24}$  selection criteria for fields of different sizes is that we have biased our redshift

distribution of SFGs and AGNs. Our selection of SFGs is predisposed toward strong PAH emitters at redshifts  $z \sim 1$  and  $z \sim 2$ , where the PAH features fall in the  $24\ \mu\text{m}$  bandpass. Strong AGNs are intrinsically brighter at  $S_{24}$  (Kirkpatrick et al. 2012); due to the smaller area of the GOODS fields, our brightest AGNs are found in the xFLS field at  $z > 2$ . However, owing to the bright detection limits, no SFGs are found at similar redshifts in xFLS. We use the IRS spectrum to determine redshifts (Section 3.2), and this introduces a bias as well, since we require coverage of PAH features or the  $9.7\ \mu\text{m}$  silicate absorption feature. In our sample, 60% of sources have coverage of the  $6\text{--}8\ \mu\text{m}$  PAH complexes, 64% have coverage of the  $11.2\text{--}12.7\ \mu\text{m}$  complexes, and 82% have coverage of the  $9.7\ \mu\text{m}$  silicate absorption feature. We have 36 sources with a featureless spectrum that have optically available redshifts, but we have rejected a further  $\sim 10\%$  of sources that meet our selection criteria because they have featureless spectra and no reliable optical redshift.

## 2.2. Spectroscopy and Photometry

Full details on the IRS observations and data reduction of the xFLS sources are discussed in Dasyra et al. (2009). Here we only present a brief summary. The data reduction starts with the *Spitzer* Basic Calibrated Data (BCD). We removed the residual median sky background from each IRS low-resolution order (the short-low (SL) order covering  $5.2\text{--}14.7\ \mu\text{m}$ , and the long-low (LL) order covering  $14.3\text{--}35.0\ \mu\text{m}$ ). We did a mixture of automatic and manual bad pixel removal, replacing their values with interpolations from their neighbors. The 1D spectra for each nod position and each spectral order were extracted using the *Spitzer* Science Center package SPICE, adopting the “optimal” extraction technique, which in essence is a weighted PSF-fitting and is recommended for faint sources. Aperture and slit-loss corrections are applied. Finally, the two nod positions are averaged and the different orders merged using linear interpolation in the overlap region. The flux calibration was found to be consistent between the orders and consistent with the broadband IRAC  $8\ \mu\text{m}$  and MIPS  $24\ \mu\text{m}$  flux densities.

The low-resolution ( $R = \lambda/\Delta\lambda \sim 100$ ) *Spitzer* IRS spectra in the GOODS-N and ECDFS fields were reduced following the method detailed in Pope et al. (2008). Specifically, since many of these are long integrations, we take care to remove latent build-up on the arrays over time, and we create a supersky from all the off-nod observations to remove the sky background. One-dimensional spectra are extracted using SPICE in optimal extraction mode. For each target, a sky spectrum is also extracted to represent the uncertainty in the final target spectrum. The target spectrum flux calibration was found to be consistent with the broadband MIPS  $24\ \mu\text{m}$  flux densities.

The xFLS field was observed with *Herschel* SPIRE as part of the HerMES survey, while the GOODS-N and ECDFS fields were imaged with *Herschel* PACS and SPIRE as part of the GOODS-*Herschel* Open Time Key Program. All *Herschel* photometric flux densities are extracted using the MIPS  $24\ \mu\text{m}$  prior positions. For sources that are blended with another galaxy based on  $24\ \mu\text{m}$  prior positions, we deblend by fitting two Gaussians. If a source is blended with two or more other galaxies, we reject the photometry at this wavelength. We also reject sources that result in a  $\leq 1\sigma$  detection. For the xFLS sources, we have rejected the  $250\ \mu\text{m}$



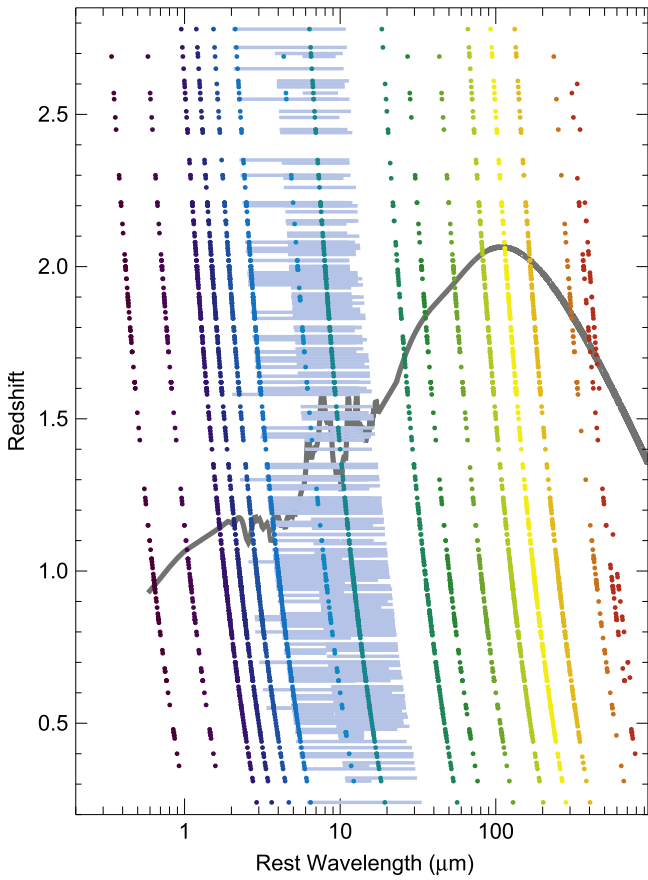


**Figure 2.** We show the available photometry and spectroscopy for each source in our sample. We redshift the observed photometric wavelengths for individual sources to the rest frame. We plot a filled circle if a source has a photometric detection at a given wavelength, and we indicate the rest frame coverage of the IRS spectra with a blue shaded region. We show an IR SED in gray to better illustrate the coverage of our photometry and spectroscopy. Our spectroscopic and photometric coverage is exceptional, and there are no significant gaps in any particular bandpass due to increasing redshift.

photometry for 23 sources, the  $350\,\mu\text{m}$  photometry for 36 sources, and the  $500\,\mu\text{m}$  photometry for 46 sources due to being too blended or too faint. In the GOODS-N and ECDFS fields, we reject 26 sources at all SPIRE wavelengths for being too blended. The sources rejected span the full redshift distribution.

We combine *Herschel* and *Spitzer* photometry and spectroscopy with ground-based near-IR and submillimeter imaging to obtain excellent coverage of the full IR spectrum from  $z=0.3$ – $2.8$ . Specifically, for the GOODS-N and ECDFS sources, we have *J*- and *K*-band photometry from VLT/ISAAC (Retzlaff et al. 2010) and CFHT/WIRCAM (Wang et al. 2010; Lin et al. 2012); *Spitzer* IRAC 3.6, 4.5, 5.8,  $8.0\,\mu\text{m}$ , IRS 16  $\mu\text{m}$ , and MIPS 24,  $70\,\mu\text{m}$  imaging; *Herschel* PACS 100,  $160\,\mu\text{m}$  and SPIRE 250,  $350\,\mu\text{m}$ ,  $500\,\mu\text{m}$  imaging; and  $870\,\mu\text{m}$  photometry from LABOCA on APEX (Weiß et al. 2009) and the combined AzTEC+MAMBO  $1.1\,\text{mm}$  map of GOODS-N (Penner et al. 2011). For the xFLS sources, we have *Spitzer* IRAC 3.6, 4.5, 5.8,  $8.0\,\mu\text{m}$ , and MIPS 24,  $70\,\mu\text{m}$ ,  $160\,\mu\text{m}$  imaging; *Herschel* SPIRE 250,  $350\,\mu\text{m}$ ,  $500\,\mu\text{m}$  imaging; and MAMBO  $1.2\,\text{mm}$  imaging (Lutz et al. 2005; Sajina et al. 2008; Martínez-Sansigre et al. 2009). We illustrate the wavelength coverage of our data in Figure 2.

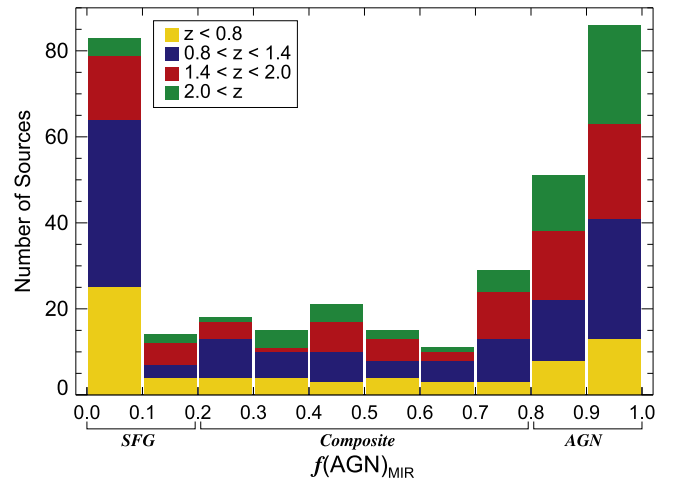


**Figure 3.** Distribution of mid-IR AGN fraction, determined from the mid-IR spectral decomposition. The colors correspond to redshift. A large portion (30%) are SFGs with little AGN contribution, but there is also a sizable population of AGNs (36%). We indicate our  $f(\text{AGN})_{\text{MIR}}$  classifications below the x-axis.

### 3. MID-IR SPECTRAL DECOMPOSITION

#### 3.1. AGN Strength

We perform spectral decomposition of the mid-IR spectrum ( $\sim 5$ – $18\,\mu\text{m}$  rest frame) for each source in order to disentangle the AGN and star-forming components. Pope et al. (2008) explain the technique in detail, and we summarize here. We fit the individual spectra with a model composed of four components: (1) the star formation component is represented by the mid-IR spectrum of the prototypical starburst M82 (we verified the choice of template by comparing with the low-redshift starburst template from Brandl et al. (2006), which produced the same results); (2) the AGN component is determined by fitting a pure power law with the slope and normalization as free parameters; (3, 4) extinction curves from the Draine (2003) dust models for Milky Way (MW) type dust are applied to the AGN component and star-forming component. The full model is then

$$S_\nu = N_{\text{AGN}} \lambda^\alpha e^{-\tau_{\text{AGN}}} + N_{\text{SF}} S_\nu(\text{M82}) e^{-\tau_{\text{SF}}}. \quad (1)$$

We fit for  $N_{\text{AGN}}$ ,  $N_{\text{SF}}$ ,  $\alpha$ ,  $\tau_{\text{AGN}}$ ,  $\tau_{\text{SF}}$ , and redshift simultaneously.

The extinction curve is not monotonic in wavelength and contains silicate absorption features, the most notable for our wavelength range being at  $9.7\,\mu\text{m}$ . It is important to note that the assumption of MW dust has a non-negligible effect on the normalization of the AGN component, and dust of lower metallicity could lower the overall contribution of an AGN to  $L_{\text{IR}}$  (Snyder et al. 2013). The M82 template already contains some intrinsic extinction. We allow additional extinction to the SF component beyond that inherent in the template and find this to be necessary for 24% of the sources.

For each source, we quantify the strength of the AGN,  $f(\text{AGN})_{\text{MIR}}$ , as the fraction of the total mid-IR luminosity coming from the extincted power-law continuum component. We classify the sources as SFGs ( $f(\text{AGN})_{\text{MIR}} < 0.2$ ), composites ( $f(\text{AGN})_{\text{MIR}} = 0.2$ – $0.8$ ), and AGNs ( $f(\text{AGN})_{\text{MIR}} > 0.8$ ). Figure 3 illustrates the  $f(\text{AGN})_{\text{MIR}}$  distribution of the sample, with colors corresponding to redshift. There are roughly equal numbers of SFGs (30%), composites (34%), and AGNs (36%).



This high percentage of AGNs is a selection effect due to the different field sizes and flux limits. Throughout the paper, we refer to these mid-IR spectroscopically identified AGNs simply as AGNs, though the reader should bear in mind that they may not be identified as such at other wavelengths.

Assessing the reliability of our decomposition technique is of utmost importance for interpreting the results in this paper. We have tested the soundness of our  $f(\text{AGN})_{\text{MIR}}$  in three ways. (1) The most serious concern is between dust extinction and AGN fraction. We find that if we remove the extinction component, 70% of our sample would have  $\Delta f(\text{AGN})_{\text{MIR}} < 0.1$ , while 21% would lie within  $\Delta f(\text{AGN})_{\text{MIR}} < 0.2$ . In general, not including the extinction component scatters to lower  $f(\text{AGN})_{\text{MIR}}$ . (2) We create synthetic spectra, where we know the input AGN fraction, and add noise. We then run our decomposition code on our synthetic spectra. We can recover  $f(\text{AGN})_{\text{MIR}}$  within 0.1 even at a signal-to-noise ratio of three. (3) We test our results by comparing to another decomposition method, *deblendIRS*, presented in Hernán-Caballero et al. (2015). The *deblendIRS* technique decomposes IRS spectra into stellar, PAH, and AGN components using a library of 19 stellar, 56 PAH, and 39 empirical AGN templates. This allows for variation in the PAH features. When comparing the two techniques, we find on average  $\Delta(f(\text{AGN})_{\text{MIR}} - f(\text{AGN})_{\text{deblendIRS}}) = 0$  with a standard deviation of 0.15. These three techniques underscore the reliability of the  $f(\text{AGN})_{\text{MIR}}$  values presented here.

### 3.1.1. Comparison of AGN Indicators

We briefly address how our AGN quantification technique compares with two other AGN selection methods often used at high redshift. Our GOODS-N and ECDFS sources have *Chandra* 2 Ms and 4 Ms (respectively) X-ray observations (Alexander et al. 2003; Luo et al. 2008; Xue et al. 2011). Of our AGNs in these fields, 73% are detected in the X-ray. We estimate that our AGNs all have comparable intrinsic X-ray luminosities, indicating that those AGNs that are not detected might be Compton-thick (Alexander et al. 2008; Bauer et al. 2010). Of our composite sources, 35% have an X-ray detection. Eleven of our AGNs are included in a study by Brightman et al. (2014) that measures column density for sources in GOODS-S. Eight of these AGNs have column densities of  $N_{\text{H}} \approx 10^{22} - 10^{23} \text{ cm}^{-2}$ , but the remaining three have  $N_{\text{H}} > 10^{24} \text{ cm}^{-2}$ , indicating Compton thickness. Much more limited X-ray data exist for the xFLS field. Specifically, Bauer et al. (2010) target 20 AGN sources with *Chandra* 150 ks observations. Only two sources are detected, and the remaining sources are estimated to be Compton-thick. Overall, there is broad agreement between our mid-IR spectral AGN indicators and X-ray AGN indicators, although we stress that our technique will not be biased against obscured AGNs, which are much more prevalent at high redshift (e.g., Treister et al. 2010).

*Spitzer* IRAC color selection is also commonly used to cull AGNs from a sample (Lacy et al. 2004; Stern et al. 2005; Donley et al. 2012). The criterion in Donley et al. (2012) is based on colors ( $S_8/S_{4.5}$  and  $S_{5.8}/S_{3.6}$ ) that distinguish whether a galaxy has power-law emission in the near- to mid-IR, and this power-law emission is indicative of an AGN. However, in Kirkpatrick et al. (2013), we demonstrated that AGNs residing in high-redshift (U)LIRGs do not universally display power-law emission in these colors due to contamination from the host galaxy. 75% of the AGNs in this sample have colors indicative of an AGN according to Donley et al. (2012), while only 29%

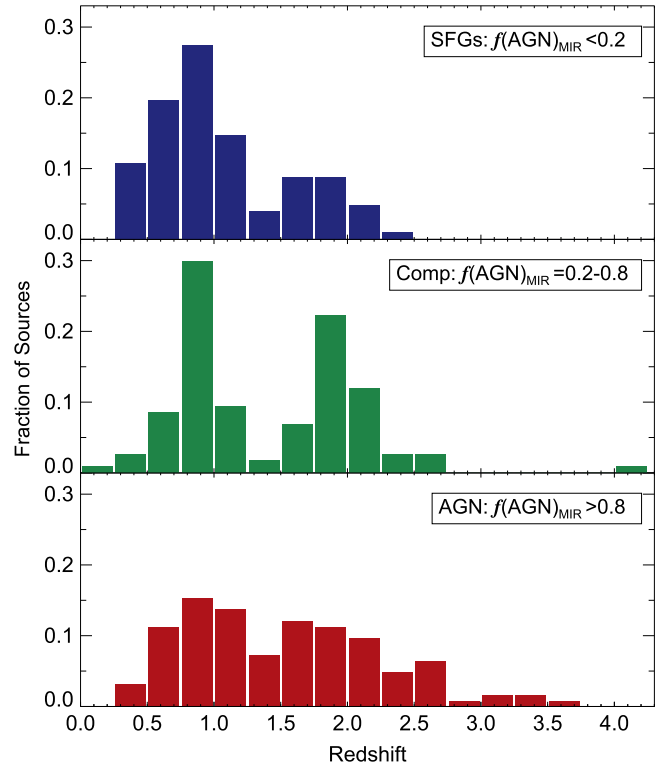


**Figure 4.** Redshift distribution of our sample where we have separated sources by  $f(\text{AGN})_{\text{MIR}}$ . The top panel shows the fraction of SFGs in each redshift bin, the middle panel shows the fraction of composites, and the bottom panel shows the fraction of AGNs per bin. The highest redshift sources are mainly AGNs, which reflects the  $24 \mu\text{m}$  selection criterion, since AGNs are typically brighter at this wavelength than SFGs. The bimodal distribution that peaks at  $z \sim 1$  and  $z \sim 2$ , particularly evident for the SFGs and composites, is also a byproduct of the  $24 \mu\text{m}$  selection, since at these redshifts prominent PAH features fall in the  $24 \mu\text{m}$  bandpass.

of composites meet these criteria. The benefit of our mid-IR spectral decomposition is that we can identify heavily obscured AGNs and *quantify* the strength of the AGN emission.

### 3.2. Spectroscopic Redshifts

We determine redshifts for the majority of our sample by fitting the positions of the main PAH features ( $6.2, 7.7, 11.2, 12.7 \mu\text{m}$  complexes). Out of our sample, 36 sources have a featureless mid-IR spectrum. In these cases, we adopt available optical spectroscopic redshifts for the GOODS/ECDFS sources (e.g., Szokoly et al. 2004; Barger et al. 2008; Popesso et al. 2009; Stern et al. 2012). Optical redshifts for the xFLS sources were determined with targeted Keck and Gemini follow-up observations (e.g., Choi et al. 2006; Yan et al. 2007; Sajina et al. 2008). Redshifts derived from fitting the PAH features have typical uncertainties of  $\Delta z = 0.01 - 0.03$  (Dasyra et al. 2009) while redshifts based only on the  $9.7 \mu\text{m}$  silicate feature (as is the case for many of our strong AGNs) have uncertainties of  $\Delta z = 0.1 - 0.2$  (Sajina et al. 2007).

The redshift distribution is illustrated in Figure 4, where we separate sources according to  $f(\text{AGN})_{\text{MIR}}$ . The redshift distribution is largely bimodal, with peaks around  $z \sim 1$  and  $z \sim 2$ , which reflects the overarching  $24 \mu\text{m}$  selection criterion. At  $z = 1, 2$ , prominent PAH features fall within the  $24 \mu\text{m}$  bandpass, causing an increase in detected sources with intense star formation. Conversely, at  $z \sim 1.5$ , the  $9.7 \mu\text{m}$  silicate absorption feature falls within the  $24 \mu\text{m}$  bandpass, resulting in

a dearth of sources. Sources with the highest redshift ( $z > 2.5$ ) are predominantly AGNs; this is also a byproduct of the  $24\ \mu\text{m}$  selection criterion since AGN activity boosts mid-IR emission. We have relatively more composites at  $z \sim 2$  than SFGs because the composites tend to be more luminous at  $24\ \mu\text{m}$  due to AGN emission and are more easily detected.

#### 4. A NEW PUBLIC LIBRARY OF EMPIRICAL INFRARED TEMPLATES

The SEDs of dusty high-redshift ULIRGs are seen to differ from the SEDs of local ULIRGs (e.g., Pope et al. 2006; Elbaz et al. 2011; Kirkpatrick et al. 2012; Sajina et al. 2012). In light of this, a library of templates designed specifically for high-redshift galaxies is required. Our large spectroscopic sample and wealth of multiwavelength data are ideally suited for this purpose. However, our individual mid-IR spectra are noisy, and many of our sources lack complete coverage of the peak of the SED emission in the far-IR, due to confusion limits from *Herschel*. Therefore, we can better study the dust emission at high redshift by considering the average SED. We combine our sources to create three libraries of *publicly available*<sup>7</sup> empirical SED templates.

1. MIR-based Library. This is a user-friendly library suited for sources with mid-IR spectroscopy.
2. Color-based Library. This is a user-friendly library ideal for sources with only IR photometry.
3. Comprehensive Library. This library best represents the intrinsic properties ( $f(\text{AGN})_{\text{MIR}}$ ,  $L_{\text{IR}}$ ) of our sources.

Within each template library, we divide our sources into subsamples using criteria outlined in Sections 4.1–4.3. Table 2 describes the basic properties of the subsamples comprising each template. We begin by shifting all spectra and photometry to the rest frame. Within each subsample, we determine the median mid-IR luminosity ( $5\text{--}15\ \mu\text{m}$ ) and scale the individual rest-frame SEDs using this value. We choose to normalize by the mid-IR luminosity because it minimizes the scatter in  $L_{\nu}$  between galaxies at all IR wavelengths while preserving the intrinsic average luminosity of each subsample.

After normalization, we average the IR data by determining the median  $L_{\nu}$  and wavelength in differential bin sizes, chosen so that each bin is well populated ( $>5$  data points). In the near-IR and far-IR, where data are scarcer, we calculate rolling medians, and we treat photometric data points and spectroscopic data points the same. For each subsample, we randomly draw sources with replacement and recalculate the normalized median 1000 times; the uncertainty on the template is then the standard deviation around the median. Because we normalize in the mid-IR, the resulting templates exhibit little scatter in and around these wavelengths.

We fit a two-temperature modified blackbody (2T MBB) to the bootstrapped far-IR data ( $>20\ \mu\text{m}$ ) and uncertainties in order to characterize the shape of the far-IR in terms of physical parameters. The 2T MBB has the form

$$S_{\nu} = a_{\text{w}} \times \nu^{\beta} \times B_{\nu}(T_{\text{w}}) + a_{\text{c}} \times \nu^{\beta} \times B_{\nu}(T_{\text{c}}), \quad (2)$$

where  $B_{\nu}$  is the Planck function, and  $T_{\text{w}}$  and  $T_{\text{c}}$  are the temperatures of the warm and cold dust components, respectively. We keep the emissivity fixed at  $\beta = 1.5$ , assuming

**Table 2**  
Categories of Template SEDs

Name	Number of Sources	Median $z$	Median $f(\text{AGN})_{\text{MIR}}$
MIR-based Templates (Figure 6)			
MIR0.0	68	0.94	0.00
MIR0.1	24	0.94	0.09
MIR0.2	21	1.10	0.20
MIR0.3	16	1.38	0.28
MIR0.4	18	1.39	0.38
MIR0.5	21	0.96	0.49
MIR0.6	15	1.59	0.60
MIR0.7	23	1.50	0.70
MIR0.8	31	1.52	0.80
MIR0.9	51	1.80	0.90
MIR1.0	54	1.18	1.00
Color-based Templates (Figure 9)			
COLOR1	75	1.10	0.14
COLOR2	57	0.94	0.23
COLOR3	41	1.17	0.39
COLOR4	26	0.95	0.77
COLOR5	29	1.52	0.81
COLOR6	25	1.09	0.96
COLOR7	24	1.97	0.87
COLOR8	23	1.83	0.94
Comprehensive Templates (Figure 11)			
SFG1	38	0.92	0.00
SFG2	23	0.91	0.00
SFG3	24	1.75	0.07
Composite1	24	0.85	0.38
Composite2	27	0.94	0.60
Composite3	18	1.89	0.43
Composite4	29	1.96	0.57
AGN1	22	0.80	1.00
AGN2	23	1.03	0.93
AGN3	21	1.65	0.94
AGN4	31	1.95	0.93

optically thin dust. The choice of model is non-trivial, and we discuss alternative far-IR models in Appendix A. We fit for the normalization factors,  $a_{\text{w}}$  and  $a_{\text{c}}$ , and the temperatures,  $T_{\text{w}}$  and  $T_{\text{c}}$ , simultaneously using a  $\chi^2$  minimization technique. The error bars in this regime reflect the uncertainty of the fitted parameters, including both the intrinsic scatter among sources and the photometric uncertainties in the data. We then verify the 2T MBB fit by overplotting photometry from  $850$  to  $1100\ \mu\text{m}$ , observed frame. The submillimeter data are not included in the fit because they are not available for the majority of sources and would therefore bias the derived cold dust temperature. For all templates, the available submillimeter data agree with the template within the photometric uncertainties. Our fitting technique is illustrated for one subsample in Figure 5, and we show all subsamples and corresponding templates in Appendix B. Table 3 lists  $T_{\text{c}}$ ,  $T_{\text{w}}$ , and  $L_{\text{IR}}$  of each template.

Other popular models for fitting the full IR SED include a power law combined with a MBB (e.g., Casey 2012) and a hot torus model combined with a 2T MBB (e.g., Sajina et al. 2012). We opt not to use these models because we do not include near- and mid-IR data in our fits as this portion of each

<sup>7</sup> <http://www.astro.umass.edu/~pope/Kirkpatrick2015>

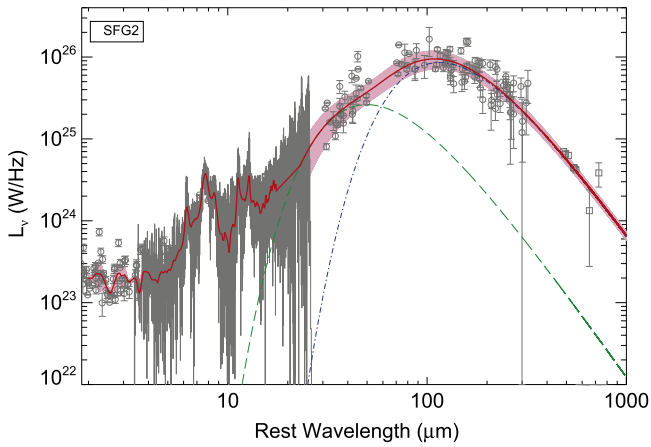


**Figure 5.** Example of our template creation technique for the SFG2 subsample (all subsamples are listed in Table 2). We show photometric and spectroscopic data (gray points and lines), and we plot the template and corresponding uncertainty in red and pink. All normalized spectroscopic and photometric data were averaged together in differential bin sizes using a bootstrapping technique to estimate the uncertainties. We then fit the far-IR averaged photometry with a 2T MBB (the green dashed line and the blue dotted-dashed line represent the warm and cold dust components, respectively). We overplot available submillimeter data ( $\lambda > 300 \mu\text{m}$ ; gray squares), *not included in the fit*, to check the validity of our 2T MBB fit. All data sets and corresponding templates are shown in Appendix B.

template is created through stacking the data. We tested what effect these different models have on measuring  $L_{\text{IR}}$  and  $T_c$  and find no significant change in these parameters.

#### 4.1. Mid-IR-based Templates

Our sample is unique in that we have mid-IR spectroscopy for every source, allowing us to classify a large sample of galaxies in a similar manner. Therefore, we create a library of eleven templates by separating sources according to  $f(\text{AGN})_{\text{MIR}}$ , in order to assess what effect a mid-IR luminous AGN has on the full IR SED. Each subsample is chosen so that it contains at least 15 sources and so that the median  $f(\text{AGN})_{\text{MIR}}$  increases by  $\sim 0.1$ , spanning the range  $f(\text{AGN})_{\text{MIR}} = 0.0$ – $1.0$ . We list the subsample properties in Table 2 and show the library of MIR-based templates in Figure 6. These user-friendly templates are ideal for inferring far-IR dust properties when little or no far-IR information is available. In particular, this template library will be useful to derive  $L_{\text{IR}}$  and estimate SFRs when mid-IR spectroscopy from the forthcoming MIRI instrument on the *James Webb Space Telescope* (JWST) becomes available.

In Figure 6, we have ordered the templates by the median  $f(\text{AGN})_{\text{MIR}}$  of the sources that comprise each template. PAH features are visible in all but the MIR1.0 template. The MIR0.8–MIR1.0 templates all exhibit silicate absorption, although this may be a selection effect since some pure power-law spectra were excluded from the final xFLS sample. In general, the MIR0.3–MIR0.7 subsamples contain fewer sources each, and these sources show a variety of SED features, which is reflected in the templates and resulting errors. The lack of uniformity in the MIR0.3–MIR0.7 templates signals that AGN emission may manifest itself in the full IR SED differently based on some property of the host galaxy, such as the spatial distribution of the dust. In contrast, the MIR0.0–MIR0.2 templates have very small uncertainties, suggesting a remarkable uniformity in shape among SFGs.

**Table 3**  
Properties of Template SEDs

Name	$T_c^a$ (K)	$T_w^a$ (K)	$L_{\text{IR}}^b$ ( $10^{12} L_\odot$ )	$L_{\text{IR}}^{\text{SF}c}$ ( $10^{12} L_\odot$ )
MIR-based Templates				
MIR0.0	$25.7 \pm 0.6$	$66.0 \pm 2.4$	$0.57 \pm 0.07$	$0.57 \pm 0.07$
MIR0.1	$26.8 \pm 1.0$	$66.7 \pm 4.5$	$0.72 \pm 0.16$	$0.69 \pm 0.15$
MIR0.2	$24.6 \pm 1.3$	$62.4 \pm 1.4$	$1.05 \pm 0.17$	$0.98 \pm 0.16$
MIR0.3	$27.3 \pm 1.9$	$75.0 \pm 11.3$	$1.22 \pm 0.52$	$1.11 \pm 0.47$
MIR0.4	$29.4 \pm 1.6$	$70.3 \pm 3.7$	$2.21 \pm 0.49$	$1.88 \pm 0.42$
MIR0.5	$29.4 \pm 1.8$	$84.3 \pm 5.6$	$1.17 \pm 0.30$	$0.92 \pm 0.23$
MIR0.6	$35.2 \pm 3.2$	$87.7 \pm 9.9$	$3.76 \pm 1.43$	$2.82 \pm 1.07$
MIR0.7	$26.1 \pm 2.2$	$80.2 \pm 3.4$	$1.95 \pm 0.47$	$1.38 \pm 0.34$
MIR0.8	$28.3 \pm 1.3$	$85.6 \pm 3.8$	$2.97 \pm 0.55$	$1.81 \pm 0.34$
MIR0.9	$29.0 \pm 1.9$	$89.8 \pm 6.1$	$3.27 \pm 0.71$	$1.67 \pm 0.36$
MIR1.0	$26.3 \pm 2.3$	$83.4 \pm 4.5$	$1.68 \pm 0.33$	$0.72 \pm 0.14$
Color-based Templates				
COLOR1	$26.4 \pm 0.9$	$63.0 \pm 4.2$	$1.16 \pm 0.25$	$1.14 \pm 0.24$
COLOR2	$24.8 \pm 1.1$	$61.5 \pm 3.4$	$0.66 \pm 0.13$	$0.59 \pm 0.12$
COLOR3	$26.9 \pm 1.5$	$62.8 \pm 4.7$	$1.89 \pm 0.49$	$1.72 \pm 0.45$
COLOR4	$20.9 \pm 1.6$	$74.3 \pm 7.4$	$0.81 \pm 0.23$	$0.52 \pm 0.15$
COLOR5	$28.5 \pm 2.4$	$80.5 \pm 4.6$	$3.35 \pm 0.85$	$2.04 \pm 0.52$
COLOR6	$27.0 \pm 2.4$	$87.3 \pm 4.6$	$1.62 \pm 0.36$	$0.66 \pm 0.15$
COLOR7	$37.0 \pm 3.3$	$88.3 \pm 7.7$	$4.82 \pm 1.66$	$2.75 \pm 0.95$
COLOR8	$24.4 \pm 2.4$	$88.9 \pm 4.1$	$2.46 \pm 0.56$	$0.81 \pm 0.19$
Comprehensive Templates				
SFG1	$26.3 \pm 1.0$	$62.4 \pm 5.9$	$0.40 \pm 0.11$	$0.38 \pm 0.10$
SFG2	$28.1 \pm 1.3$	$64.9 \pm 5.6$	$1.31 \pm 0.35$	$1.27 \pm 0.34$
SFG3	$26.8 \pm 1.8$	$58.1 \pm 6.9$	$1.35 \pm 0.51$	$1.28 \pm 0.49$
Composite1	$25.7 \pm 0.9$	$81.0 \pm 5.0$	$0.49 \pm 0.09$	$0.45 \pm 0.08$
Composite2	$30.9 \pm 2.7$	$84.3 \pm 4.6$	$1.31 \pm 0.51$	$1.05 \pm 0.41$
Composite3	$31.1 \pm 2.8$	$72.5 \pm 9.6$	$1.60 \pm 0.72$	$1.02 \pm 0.46$
Composite4	$38.9 \pm 2.9$	$82.8 \pm 15.6$	$6.96 \pm 3.34$	$5.01 \pm 2.40$
AGN1	$21.7 \pm 2.2$	$72.7 \pm 7.6$	$0.47 \pm 0.17$	$0.21 \pm 0.08$
AGN2	$25.3 \pm 2.9$	$86.0 \pm 4.4$	$2.03 \pm 0.58$	$1.24 \pm 0.35$
AGN3	$31.8 \pm 4.1$	$78.5 \pm 9.8$	$2.38 \pm 1.18$	$0.90 \pm 0.45$
AGN4	$33.4 \pm 5.3$	$75.2 \pm 5.8$	$6.57 \pm 2.10$	$3.22 \pm 1.03$

#### Notes.

<sup>a</sup> See Equation (2).

<sup>b</sup> Calculated by integrating each template from 8 to  $1000 \mu\text{m}$ .

<sup>c</sup> Fraction of  $L_{\text{IR}}$  attributable to star formation. Calculated total AGN contribution to  $L_{\text{IR}}$ ,  $f(\text{AGN})_{\text{total}}$ , and scaled  $L_{\text{IR}}$  correspondingly to obtain  $L_{\text{IR}}^{\text{SF}}$ . See Section 5.

The MIR0.0–MIR0.2 templates are consistent in shape with the  $z \sim 1$  SF SED and  $z \sim 2$  SF SED from Kirkpatrick et al. (2012). The Silicate AGN SED from Kirkpatrick et al. (2012), created from sources with  $f(\text{AGN})_{\text{MIR}} > 0.5$  that exhibited silicate absorption at  $9.7 \mu\text{m}$ , is consistent with the MIR0.6 template. In contrast, the Featureless AGN SED from that work, created from sources with  $f(\text{AGN})_{\text{MIR}} > 0.5$  with a power-law spectrum, is not consistent with any of the templates presented here. The MIR0.8–MIR1.0 templates all have more cold dust emission than we observed previously. By combining the GOODS+ECDFS sources from Kirkpatrick et al. (2012) with the xFLS sources from Sajina et al. (2012), we more than doubled the number of AGNs in the sample, increasing the range of observed far-IR SEDs. We also now have proportionally more AGNs with silicate absorption, rather than pure



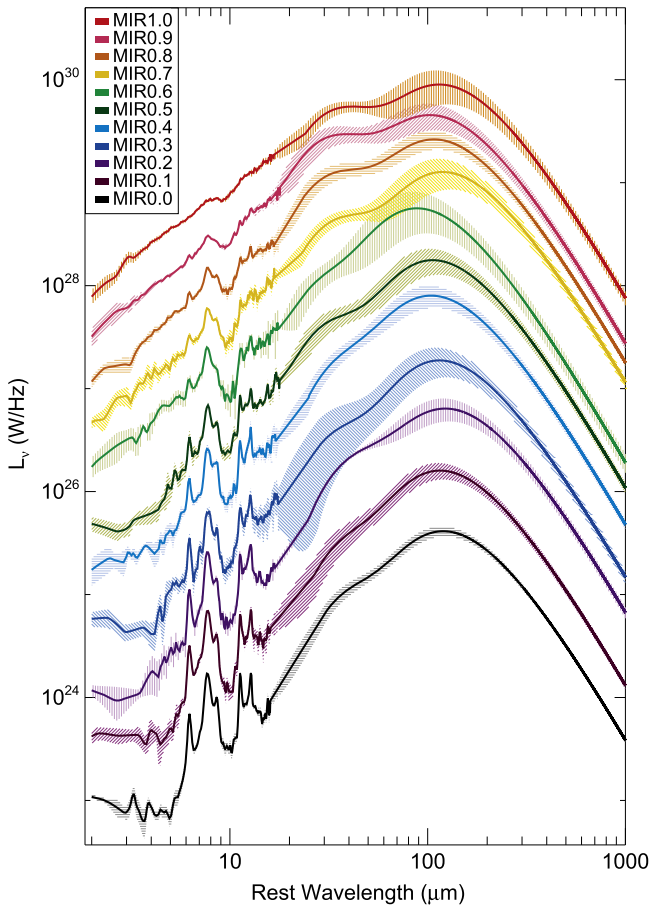


**Figure 6.** MIR-based Template Library created by grouping sources according to  $f(\text{AGN})_{\text{MIR}}$  to explore how the shape of the IR SED changes as an AGN grows more luminous. Template subsample properties are listed in Table 2. The templates have been arbitrarily offset in  $L_\nu$  to allow for easier comparison. Shaded regions show the uncertainties for each template. MIR0.3 has particularly large uncertainties around  $20\ \mu\text{m}$ , but this is due to a lack of data points in this regime. As the mid-IR AGN grows stronger, the far-IR emission becomes flatter due to an increase in the warm dust emission.

power-law AGNs, and these silicate AGNs tend to have more cold dust.

We characterize the shape of the far-IR using  $T_c$ ,  $T_w$ , and  $L_{\text{cold}}/L_{\text{IR}}$  and plot these properties as functions of  $f(\text{AGN})_{\text{MIR}}$  (median of each subsample) in Figure 7.  $L_{\text{cold}}$  is derived by integrating under the cold dust MBB from Equation (2), and it arises from the diffuse ISM, making  $L_{\text{cold}}$  and  $T_c$  secure tracers of the host galaxy (Dunne & Eales 2001).  $T_c$  varies by less than 5 K for almost all templates (gray dashed line is median  $T_c$ ), illustrating that  $T_c$ , which quantifies the peak wavelength of the dust emission, is not correlated with the presence of a mid-IR luminous AGN. Since  $T_c$  arises from the diffuse ISM, this indicates that, on average, the galaxies in our sample all display extended dust emission.  $T_c$  for MIR0.6 (light green) is a notable exception.  $T_c$  is nearly 10 K higher for this template, shifting the peak of the SED from  $\sim 110$  to  $\sim 90\ \mu\text{m}$ .  $T_c$  is higher for MIR0.6 due to a combination of the fact that there are fewer sources in this bin and these are the most luminous sources on average in the sample. It is possible this subsample is made up of more compact galaxies, leading to higher overall dust temperatures. We explore correlations between  $T_c$  and  $L_{\text{IR}}$  in Section 4.3.

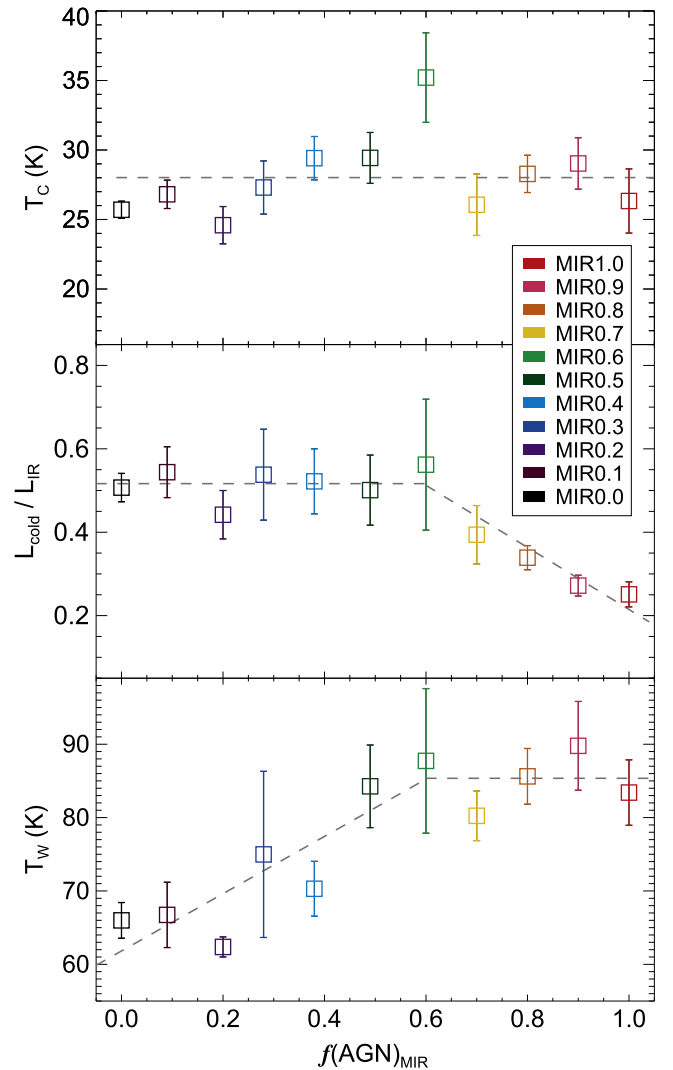


**Figure 7.** Cold dust temperature (top panel),  $L_{\text{cold}}/L_{\text{IR}}$  (middle panel), and warm dust temperature (bottom panel) as a function of  $f(\text{AGN})_{\text{MIR}}$  for the MIR-based templates.  $f(\text{AGN})_{\text{MIR}}$  is the median value of the sources comprising each template.  $T_w$  increases until  $f(\text{AGN})_{\text{MIR}} = 0.6$ , while  $L_{\text{cold}}/L_{\text{IR}}$  decreases after this point. In contrast,  $T_c$  is roughly constant (dashed line is median  $T_c$ ).

$L_{\text{cold}}/L_{\text{IR}}$ , the fraction of  $L_{\text{IR}}$  due to cold dust emission, is nearly constant for the MIR0.0–MIR0.6 templates, after which it starts to decrease (middle panel of Figure 7). We illustrate this trend with the gray dashed line, where we join the median  $L_{\text{cold}}/L_{\text{IR}}$  for MIR0.0–MIR0.6 with a simple linear fit to the MIR0.6–MIR1.0 points. Until  $f(\text{AGN})_{\text{MIR}} = 0.6$ , emission from the extended host galaxy is dominating the infrared luminosity, despite a growing contribution from an AGN to the mid-IR.

In contrast,  $T_w$  increases until  $f(\text{AGN})_{\text{MIR}} = 0.6$ , and then it is fairly constant for  $f(\text{AGN})_{\text{MIR}} = 0.7$ – $1.0$  (bottom panel; dashed line is a linear fit joined to a median).  $T_w$  has two possible heating sources. The first is star-forming regions, either in the extended disk or in a compact starburst, although locally compact starbursts are measured to produce higher temperatures (e.g., Díaz-Santos et al. 2011). In the MIR0.0–MIR0.1 templates,  $T_w$  can be safely attributed to star formation. As the AGN grows stronger, it will contribute to  $T_w$ , eventually outshining any dust heated by star formation. The gas that fuels

a growing AGN can fuel a compact starburst too, making it difficult to distinguish exactly what is responsible for high  $T_w$  values. However, the clear trend between  $T_w$  and  $f(\text{AGN})_{\text{MIR}}$  in our sample indicates that either the AGN progressively increases its heating contribution to the wavelength range  $\lambda = 20\text{--}80\ \mu\text{m}$ , producing higher  $T_w$  values, or the growth of the AGN is directly linked with a compact starburst that is responsible for the boost in  $T_w$ .  $f(\text{AGN})_{\text{MIR}} = 0.6$  marks a turning point in the shape of the IR SED. It is here that  $T_w$  reaches its peak, and afterwards AGN-heated dust contributes more to  $L_{\text{IR}}$  than the diffuse dust heated by star formation.

The warm dust component fits to the wavelength range  $\sim 20\text{--}80\ \mu\text{m}$  which, for our sample, is covered by MIPS and PACS observations. The xFLS sources lack PACS detections, which could affect the reliability of the warm dust fits and the trend between  $T_w$  and  $f(\text{AGN})_{\text{MIR}}$ . We test how reliable the trend is by fitting the 2T MBB to the far-IR data after removing all PACS and MIPS 160 (available for a few xFLS sources) photometry. The same trends between  $T_w$ ,  $L_{\text{cold}}/L_{\text{IR}}$ , and  $f(\text{AGN})_{\text{MIR}}$  are observed.

#### 4.2. Color-based Templates

In the MIR-based Template Library, we grouped sources according to  $f(\text{AGN})_{\text{MIR}}$ , but as we noted, the individual sources comprising some of the templates showed a broad range of observed SED properties. We now explore an alternative way to sort sources and create templates based only on the SED shape of each source. In Kirkpatrick et al. (2013) we created an IR color diagnostic designed to capture the full shape of the SED by combining far-, mid-, and near-IR photometry. We present this color diagnostic in Figure 8, where we make use of photometry from *Herschel* SPIRE and *Spitzer* MIPS/IRAC, available for 87% of our sample.  $S_{250}/S_{24}$  (observed) traces the ratio of far-IR emission to mid-IR emission, and this ratio is lower in AGN sources as the heating from the AGN boosts the mid-IR emission. At the redshifts of our sources,  $S_8/S_{3.6}$  (observed) is primarily tracing the stellar bump, and in this regime, radiation from the AGN washes this feature out, producing power-law emission.

The top panel of Figure 8 illustrates that  $f(\text{AGN})_{\text{MIR}}$  grows larger with decreasing  $S_{250}/S_{24}$  and increasing  $S_8/S_{3.6}$ . There is a degree of scatter, particularly among the AGN sources, and in Kirkpatrick et al. (2013) we demonstrated that much of this scatter is attributable to the broad redshift range of our sources. However, intrinsic SED shape can also produce scatter, and we have tested this effect using the library of torus models in Siebenmorgen et al. (2015). These models account for the intrinsic luminosity of the AGN, the viewing angle, the inner radius of the torus, the volume filling factor and optical depth of the toroidal clouds, and the optical depth of the disk midplane in the host galaxy. We redshift the models to  $z = 1.5$  and plot their observed frame colors. We find that this library of AGN SEDs occupies the same general region as our AGNs, although with a much broader distribution of colors, and varying the radius of the inner torus and the optical depth of the host disk does the best job at reproducing the observed scatter of our sources. Modeling the geometry of the torus in individual sources is beyond the scope of this work; however, the above suggests that allowing for a range of host galaxy optical depths can already account for much of the scatter in colorspace. Indeed, E. Roebuck et al. (2016, in preparation) uses simulations to show that our empirical IR AGN templates

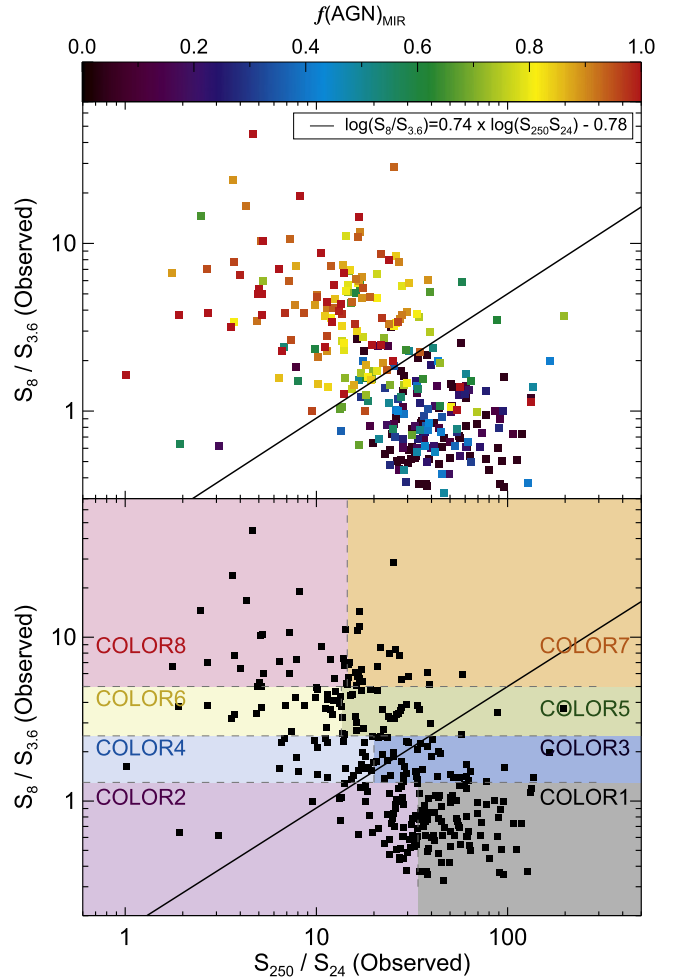


**Figure 8.** Distribution of our sources in IR colorspace using the observed frame colors. Top panel—each source is shaded according to  $f(\text{AGN})_{\text{MIR}}$ . AGN strength increases as  $S_{250}/S_{24}$  decreases and  $S_8/S_{3.6}$  increases. The dark line (equation in upper right corner) shows the empirical separation between the AGN and SFGs defined in Kirkpatrick et al. (2013). Bottom panel—for the color-based templates, we group sources by their location in colorspace in order to better explore the differences in the intrinsic IR SED shapes. The sources that comprise each template are illustrated by the shaded regions.

include not only the torus, but also the host dust-reprocessed light. We conclude that both redshift and intrinsic SED shape can account for the scatter of our sample.

To create the color-based templates, we divide sources according to  $S_{250}/S_{24}$  and  $S_8/S_{3.6}$ , so that we can quantify differences in  $T_w$  and  $T_c$  as a smooth function of  $S_{250}/S_{24}$  and  $S_8/S_{3.6}$ . We illustrate the color criteria for each subsample in the bottom panel of Figure 8. We have blindly chosen the color criteria rather than basing them on existing knowledge of the IR SED so that we can more fairly test how SED properties correlate with colors. The color bins were chosen so that each subsample has roughly the same number of sources. This template library is ideal for applying to high-redshift sources that only have IR photometry available. Although created from the same sources, this library differs from the MIR-based Library in part because  $S_8/S_{3.6}$  is sensitive to dust obscuration which is an effect missed when separating by  $f(\text{AGN})_{\text{MIR}}$  alone. Furthermore,  $S_{250}/S_{24}$  is sensitive to dust temperature, and when we sort sources by this color, we can test how strong the link is between the increase in warm dust and  $f(\text{AGN})_{\text{MIR}}$ . This is subtly different from linking  $T_w$  and  $f(\text{AGN})_{\text{MIR}}$  in the

**Table 4**  
Mid-IR AGN Strength of IR Color Regions

Region <sup>a</sup>	$S_8/S_{3.6}$ <sup>b</sup>	$S_{250}/S_{24}$ <sup>b</sup>	Mean $f(\text{AGN})_{\text{MIR}}$	$\sigma^c$
COLOR1	<1.3	$\geq 35$	0.20	0.24
COLOR2	<1.3	<35	0.26	0.27
COLOR3	1.3–2.5	$\geq 20$	0.41	0.34
COLOR4	1.3–2.5	<20	0.70	0.26
COLOR5	2.5–5.0	$\geq 13.5$	0.75	0.27
COLOR6	2.5–5.0	<13.5	0.94	0.06
COLOR7	$\geq 5.0$	$\geq 14.5$	0.83	0.12
COLOR8	$\geq 5.0$	<14.5	0.91	0.10

**Notes.**

<sup>a</sup> Each region is illustrated in the bottom panel of Figure 8.

<sup>b</sup> The color limits corresponding to each region.

<sup>c</sup> The standard deviation of  $f(\text{AGN})_{\text{MIR}}$  around the mean values so that the reader can understand the typical spread of  $f(\text{AGN})_{\text{MIR}}$  for each region.

MIR-based Library. In essence, with the MIR-based Library, we sorted sources by mid-IR AGN emission and looked for trends with the far-IR. Here, we begin by separating according to a far-/mid-IR color and test whether we recover the same trends with  $f(\text{AGN})_{\text{MIR}}$ .

In Kirkpatrick et al. (2013), we defined an empirical separation between AGNs and SFGs

$$\log(S_8/S_{3.6}) = 0.74 \times \log(S_{250}/S_{24}) - 0.78 \quad (3)$$

shown as the dark line in Figure 8. By dividing colorspace into eight quadrants, we can refine this AGN selection technique to include composites as well. Our color criteria can be used to estimate  $f(\text{AGN})_{\text{MIR}}$  of a source, and for this purpose we list the mean  $f(\text{AGN})_{\text{MIR}}$  in each color region in Table 4. The upper three quadrants, COLOR6, COLOR7, and COLOR8, have the smallest spread of  $f(\text{AGN})_{\text{MIR}}$ , so these color criteria are excellent for selecting strong AGN sources. SFGs are confined to the lower three quadrants, COLOR1, COLOR2, and COLOR3. The middle regions, COLOR4 and COLOR5, have a large population of composite galaxies, which show strong star-forming and AGN signatures.

Figure 8 and Table 4 demonstrate that there is a large spread in the observed colors of AGNs due to differing levels of dust obscuration, varying amounts of dust heating by the AGN, or slight differences in the intrinsic SED of the host galaxy (Mullaney et al. 2011). We have tested potential effects of heavy obscuration using the high- $\tau$  AGN template from Sajina et al. (2012) and find that obscuration can account for some of the scatter in the COLOR6, COLOR7, and COLOR8 quadrants, but it will not cause an AGN to mimic the colors of an SFG or composite. The spread in our AGN SEDs is consistent with what is observed in the local universe, where local LIRGs with a significant mid-IR AGN contribution have a larger range of silicate absorption and PAH emission strengths compared with star-forming LIRGs (Stierwalt et al. 2014).

We show all eight templates in Figure 9, where we have separated the templates into two panels for easier comparison based on  $S_{250}/S_{24}$  color divisions. For consistency with the other libraries, we also truncate these templates below  $2 \mu\text{m}$ , although the observed  $3.6 \mu\text{m}$  photometry point falls below this threshold at  $z > 0.8$ . In general, there is a lot of scatter below  $2 \mu\text{m}$ , and since we are not fitting this regime with any physical

model, we truncate the templates to avoid over-interpreting the data. The templates in the right panel, with higher  $S_{250}/S_{24}$  ratios, all have clearly visible PAH features. In the left panel, the warm dust component is clearly prominent, and the near-IR slope grows steeper as the AGN becomes stronger. The COLOR8 template still has larger errors around the cold dust component than the other templates, which is primarily attributable to selection effects. This template is composed of the strongest AGN sources, and these sources typically lie at higher redshift, producing less photometry in the Rayleigh–Jeans tail (at the median redshift,  $500 \mu\text{m}$  observed frame corresponds to  $\sim 170 \mu\text{m}$  rest frame). The cold dust emission of this template agrees with the available submillimeter observations (Appendix B), but since submillimeter observations are necessarily biased toward colder sources, we caution against using this template to extrapolate to submillimeter wavelengths.

We explore the dust properties as a function of the IR colors in Figure 10. By grouping sources based on observed properties, we are able to look for correlations between observed properties and intrinsic properties such as dust temperature and  $f(\text{AGN})_{\text{MIR}}$ . The cold dust temperature shows no obvious correlation with  $S_{250}/S_{24}$  and  $S_8/S_{3.6}$ . This is similar to what we observe for the MIR-based Library.  $S_{250}/S_{24}$  is correlated with  $T_w$  and  $L_{\text{cold}}/L_{\text{IR}}$ . The trend with  $S_{250}/S_{24}$  is expected since this ratio covers the wavelength range where we fit the warm MBB. The trend with  $L_{\text{cold}}/L_{\text{IR}}$  clearly demonstrates that  $S_{250}/S_{24}$  is a good proxy for the relative amount of cold dust emission by a galaxy.

We are also able to observe the effect of the AGN on multiple portions of the IR SED when we examine the trends between  $L_{\text{cold}}/L_{\text{IR}}$ ,  $T_w$ , and the near-IR color  $S_8/S_{3.6}$ . The prominence and temperature of the warm dust component increase as this color increases. The increase of  $S_8/S_{3.6}$  is due to dust heating from the torus outshining the stellar bump, producing a power law whose slope depends on the amount of dust extinction. The far-IR emission is not necessarily occurring on the same spatial scales as the near-IR emission, since dust at different temperatures is required to produce emission in each wavelength range. The correlation between  $L_{\text{cold}}/L_{\text{IR}}$ ,  $T_w$ , and  $S_8/S_{3.6}$  could indicate that the same mechanism is responsible for both far-IR and near-IR sources of dust heating. We can test whether an AGN or star formation is the primary driver of the warm dust temperature by comparing the warm dust temperature with the amount of  $L_{\text{IR}}$  due to star formation or an AGN (calculated in Section 5). We find no correlation between  $T_w$  and  $L_{\text{IR}}^{\text{SF}}$  (listed in Table 3), but we see a strong relationship between  $T_w$  and  $L_{\text{IR}}^{\text{AGN}}$ , hinting that AGN luminosity is responsible for the increase in the warm dust temperature. This AGN-heated warm dust cannot be directly associated with the torus, which is on much smaller spatial scales and much hotter, but is most likely AGN-heated dust in the host galaxy.

The bottom row of Figure 10 shows the trends between  $f(\text{AGN})_{\text{MIR}}$  and each color. We plot the median  $f(\text{AGN})_{\text{MIR}}$  and include the upper and lower quartiles to illustrate the spread in each subsample.  $f(\text{AGN})_{\text{MIR}}$  is strongly correlated with  $S_{250}/S_{24}$ , illustrating that the ratio of far- to mid-IR emission is an excellent indicator of mid-IR AGN strength. On the other hand,  $f(\text{AGN})_{\text{MIR}}$  shows a bimodality with  $S_8/S_{3.6}$  rather than a linear trend. Sources with  $f(\text{AGN})_{\text{MIR}} > 0.8$  have a range of  $S_8/S_{3.6}$  values, partially explained by differing



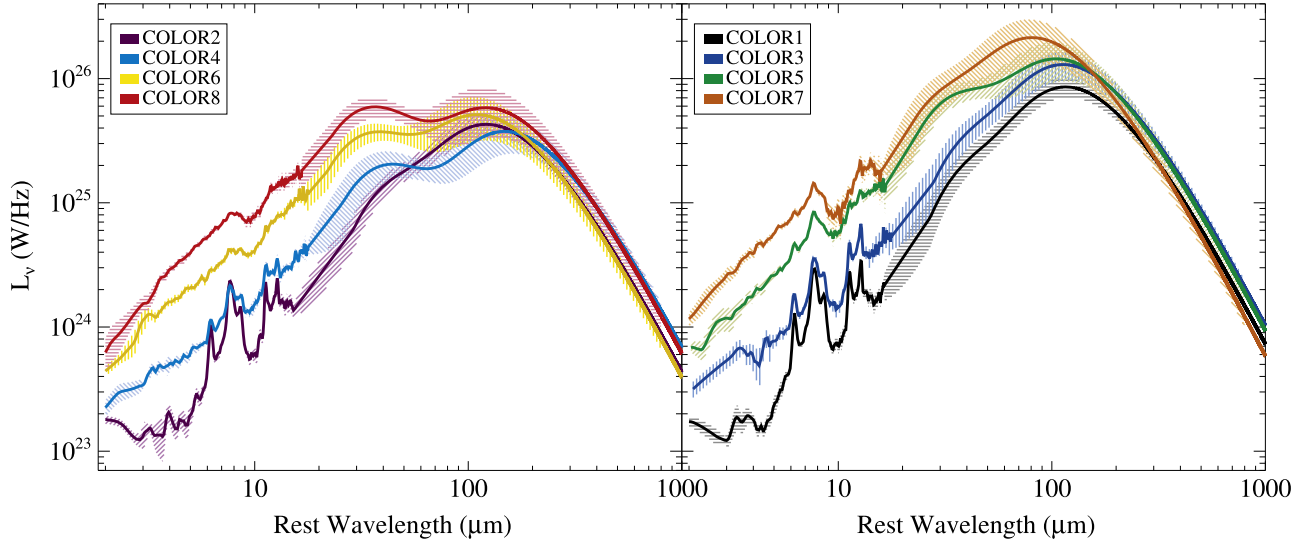


**Figure 9.** Color-based Template Library. The sources have been selected by their location in IR colorspace. We have separated the eight templates into two panels to allow for easier comparison based on their far-IR colors. The templates in the left panel have lower  $S_{250}/S_{24}$  ratios and a stronger warm dust contribution than the templates in the right panel.

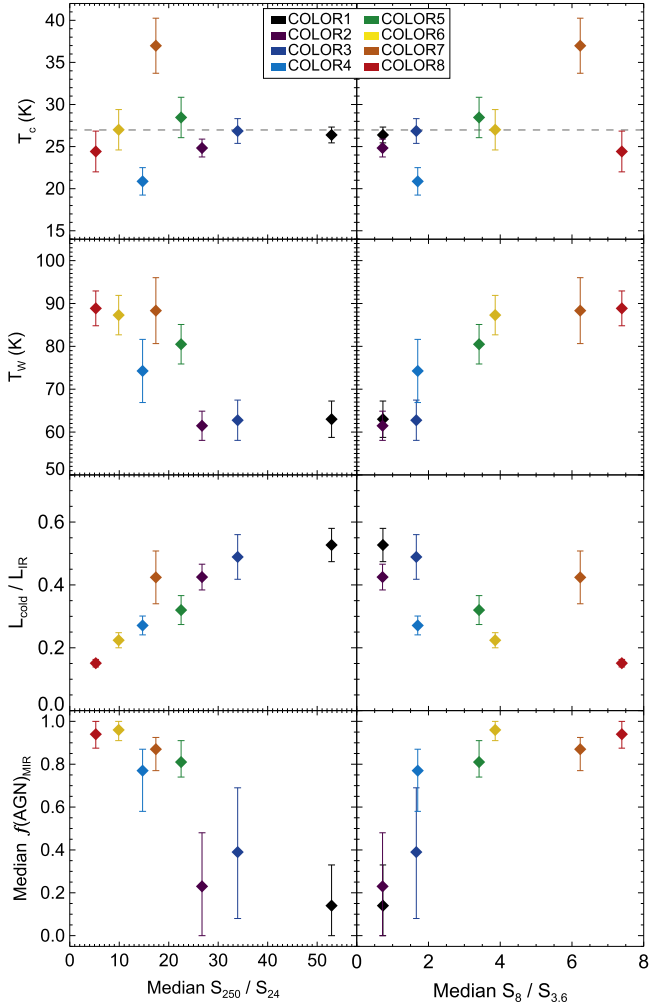


**Figure 10.** Dust properties of the Color-based Templates. Warm dust temperature,  $L_{\text{cold}}/L_{\text{IR}}$ , and  $f(\text{AGN})_{\text{MIR}}$  are strong functions of the two IR colors, due to the fact that  $T_w$  and  $L_{\text{cold}}/L_{\text{IR}}$  are influenced by heating from the growing AGN. In contrast, the cold dust temperature comes from the host galaxy, and this property is insensitive to IR color.

extinction levels, while sources with  $f(\text{AGN})_{\text{MIR}} < 0.2$  have  $S_8/S_{3.6} \leq 1$ .

#### 4.3. Comprehensive Templates

In this library, we look for evolution of the IR SED shape as a function of AGN strength, redshift, and  $L_{\text{IR}}$ . We initially separate our sources by  $f(\text{AGN})_{\text{MIR}}$ . We have three categories: (1) SFGs ( $f(\text{AGN})_{\text{MIR}} \leq 0.2$ ); (2) Composites ( $f(\text{AGN})_{\text{MIR}} = 0.2-0.8$ ); (3) AGNs ( $f(\text{AGN})_{\text{MIR}} \geq 0.8$ ). These categories are motivated by the trends we seen in the MIR-based and Color-based Libraries. The bottom panels of Figure 10 demonstrate that the near-IR and far-IR colors change significantly when  $f(\text{AGN})_{\text{MIR}} > 0.8$  and  $f(\text{AGN})_{\text{MIR}} < 0.2$ , making these natural selection thresholds.

Within these  $f(\text{AGN})_{\text{MIR}}$  categories, we further separate by redshift and by  $L_{\text{IR}}$ , selected to maximize completeness in each  $L_{\text{IR}}-z$  bin. We have optimized the redshift and  $L_{\text{IR}}$  selection criteria in order to have at least two subsamples with similar median redshifts and two subsamples with similar  $L_{\text{IR}}$  values, so that we can examine the shape of the templates as a function of both redshift and  $L_{\text{IR}}$ . The division of the sources is illustrated in the top rows of Figure 11. Our Comprehensive Library is shown in the middle rows of Figure 11, and in the bottom rows we have normalized the templates at  $300 \mu\text{m}$  to allow for easier comparison. The large uncertainties in the range  $15-30 \mu\text{m}$  for the higher redshift templates are due to a scarcity of photometric data, particularly for the SFGs due to these sources being intrinsically fainter in this regime. The high-redshift Composites (blue and gold templates) have large far-IR errors as a result of few sources in this subsample. In contrast, the large uncertainties on the far-IR for the AGN templates are caused by the intrinsic scatter of SED shapes among these subsamples and a lack of data constraining the Rayleigh-Jeans tail for the high-redshift templates.

The bottom panels of Figure 11 qualitatively illustrate a fundamental difference between our SFGs and our Composites and AGNs. The SFGs have a high degree of similarity between all  $L_{\text{IR}}$ s and redshifts. Our analysis suggests that, on average,

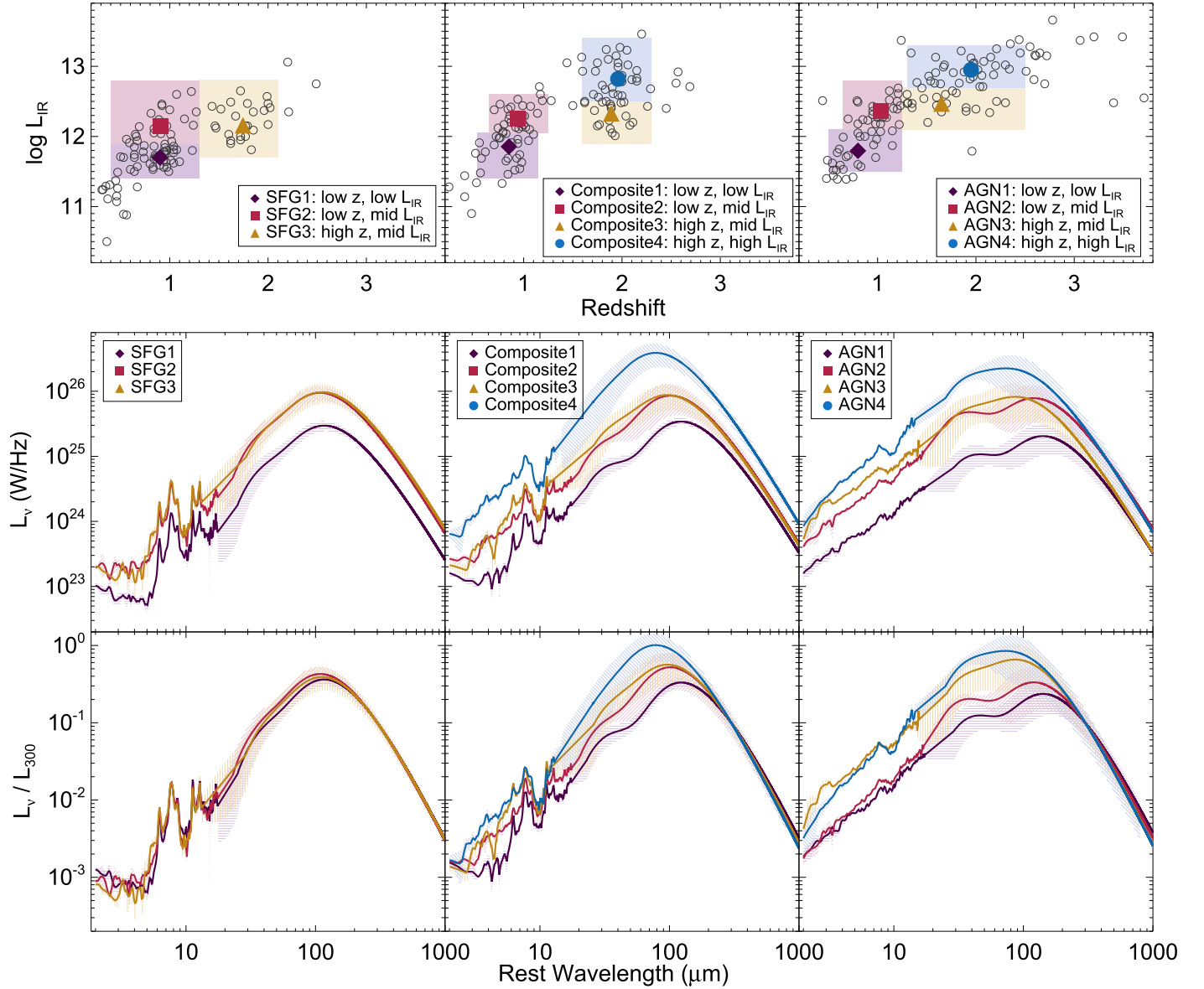


**Figure 11.** We present our library of Comprehensive Templates where we have separated sources by  $f(\text{AGN})_{\text{MIR}}$ , redshift, and  $L_{\text{IR}}$ . SFGs ( $f(\text{AGN})_{\text{MIR}} < 0.2$ ) are plotted in the left column, Composites ( $f(\text{AGN})_{\text{MIR}} = 0.2\text{--}0.8$ ) in the middle column, and AGNs ( $f(\text{AGN})_{\text{MIR}} > 0.8$ ) in the right column. The top row shows our selection criteria as the shaded regions for the sources that comprise each template. We overplot the median  $L_{\text{IR}}$  and  $z$  in each subsample (symbols here correspond to symbols used in Figure 12). Shaded regions were selected to maximize completeness while optimizing the median redshift and  $L_{\text{IR}}$  so that we can compare templates at similar redshifts and  $L_{\text{IR}}$ . The middle row shows the library of templates at the intrinsic luminosity density of each template, while in the bottom row the templates have all been normalized at  $300\ \mu\text{m}$  to allow easier comparison of the mid- and far-IR features. The large uncertainties on the far-IR emission of the AGN templates are due to the intrinsic scatter of SED shapes among these sources and a lack of data constraining the Rayleigh–Jeans tail due to the redshifts of the sources. The shape of the SFGs is remarkably consistent. The peak of the SED increases steadily for the Composites, as can clearly be seen in the bottom middle panel. The AGN1 and AGN2 templates, which are created from the lower redshift AGNs, have a distinctly different far-IR shape than the AGN3 and AGN4 templates, indicating a possible evolution of temperature with redshift.

the SFG SED does not evolve with redshift or luminosity for these types of massive dusty galaxies. Any evolution between  $L_{\text{IR}}$  and dust temperature is driven not by an intrinsic change in the ISM of high-redshift (U)LIRGs, but by a different process, such as a growing AGN. We should note that our selection criterion is biased toward sources with strong PAH emission (which we will comment on further in Section 6), and we are examining only one order of magnitude in  $L_{\text{IR}}$ , which is possibly too narrow a range to expect to see any strong trend between  $T_c$  and  $L_{\text{IR}}$ .

We quantify the far-IR dust properties of the Comprehensive Library in Figure 12. In the left column, we plot  $T_c$ ,  $T_w$ , and

$L_{\text{cold}}/L_{\text{IR}}$  as functions of the median redshift of the sources that were used to create each template. In the right column, we plot these properties as functions of template  $L_{\text{IR}}$ . The three SFG templates all have the same  $T_c$ ,  $T_w$ , and  $L_{\text{cold}}/L_{\text{IR}}$  regardless of  $L_{\text{IR}}$  or redshift, effectively demonstrating the lack of evolution in these sources, on average.

In contrast, the Composites and AGNs show a clear increase in  $T_c$ , also evident in Figure 11 where the peak of the SED shifts with increasing  $L_{\text{IR}}$  and  $z$ . For the Composites, the increase in  $T_c$  is correlated with  $L_{\text{IR}}$ , as can be seen clearly by examining the green points in the top right panel of Figure 12. The Composite2 and Composite4 templates (square and circle)

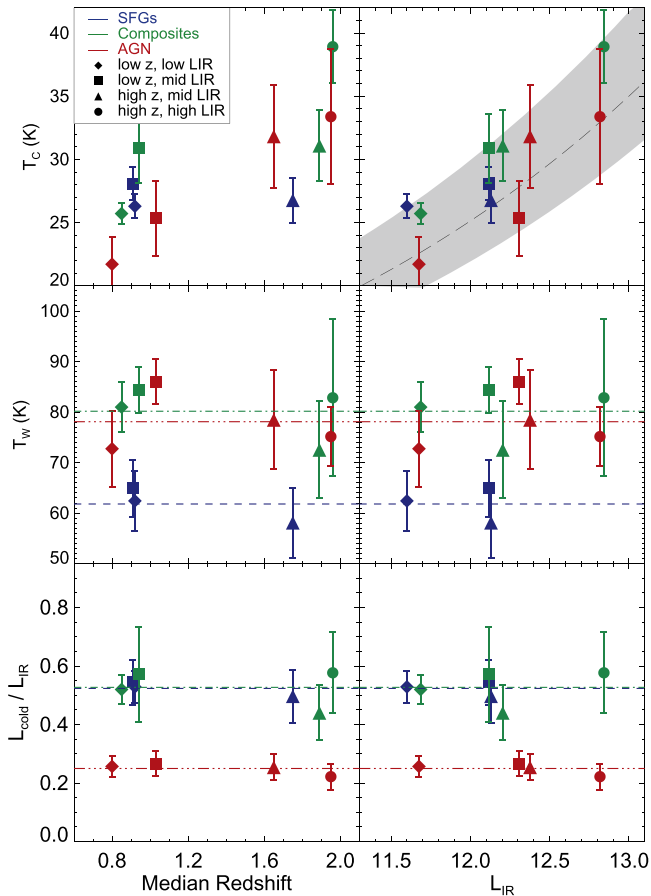


**Figure 12.** We plot the derived cold and warm dust temperatures ( $T_c$ ,  $T_w$ ) for each of our 11 Comprehensive Templates, as well as the fraction of  $L_{\text{IR}}$  due to the cold dust component. We shade the points according to  $f(\text{AGN})_{\text{MIR}}$ , so that SFGs are blue, Composites are green, and AGNs are red; in addition, symbols correspond to redshift and  $L_{\text{IR}}$  of the templates (illustrated in the top row of Figure 11). Here, we plot the far-IR dust parameters as a function of the median redshift of the sources used to create each template and as a function of the template  $L_{\text{IR}}$ . In the lower panels, we plot the median  $T_w$  and  $L_{\text{cold}}/L_{\text{IR}}$  for the SFGs, Composites, and AGN templates as the dashed lines. Cold dust temperature increases with  $L_{\text{IR}}$  and redshift for the Composites and AGNs, while the SFGs show no evolution.  $L_{\text{cold}}/L_{\text{IR}}$  is significantly lower in the AGN templates because dust heated by the AGN is now outshining much of the dust heated by starlight alone. In the upper right panel, we have plotted the  $L_{\text{IR}}-T$  relation from Casey et al. (2012).

each have  $T_c$  at least 5 K higher than the respective Composite1 and Composite3 templates (diamond and triangle), despite lying at similar redshifts. In contrast, for the AGNs, the increase of  $T_c$  is more strongly correlated with redshift, although  $T_c$  has large uncertainties. It is important not to overstate this distinction, since our high-redshift subsamples are biased toward sources with high  $L_{\text{IR}}$ . Nevertheless, the clear difference between the AGNs and Composites hints that different mechanisms could be driving the evolution of dust temperature. For the Composites, this change could be driven by an increase in the importance of mergers, which produce compact starbursts and warmer dust (Armus et al. 2007), while for the AGNs, there might be an intrinsic evolution in the effect of an AGN on the IR SED with redshift, as galaxies have higher gas fractions and clumpier ISMs. We have morphological classifications for our xFLS sample (Zamojski et al. 2011), and these data hint at an increase in the number of interacting galaxies for the higher luminosity Composite

templates, but not for the AGNs. We will examine the individual morphologies of our galaxies in a future work.

The relationship between dust temperature and  $L_{\text{IR}}$  that we see for the Composites and AGNs is consistent with what is derived for a large sample of high-redshift SPIRE 250  $\mu\text{m}$  selected galaxies (Casey et al. 2012). We have overplotted the relation from Casey et al. (2012) as the black line and gray shaded region in the top right panel of Figure 12. Casey et al. (2012) make no attempt to separate sources into SFGs or AGNs. The increase in  $T_c$  in our Composite and AGN templates is noticeably absent in our SFG templates, implying that the  $L_{\text{IR}}-T$  relation is not driven by a simple change in the ISM with redshift. However, we lack a higher luminosity SFG template, so it is impossible to say conclusively that we would not observe a trend among the SFGs if we had full coverage at high  $L_{\text{IR}}$ .

The middle panels of Figure 12 show the warm dust temperatures. We plot the average warm dust temperatures for the SFG, Composite, and AGN templates as the dashed lines to allow for easier comparison.  $T_w$  does not evolve strongly with either  $L_{\text{IR}}$  or redshift. Furthermore,  $T_w$  is similar for the Composite templates (the average  $T_w$  for all four templates is 80 K) and AGN templates (average  $T_w = 78$  K), while SFGs have a lower average  $T_w$  of 62 K. This suggests that the mechanism responsible for heating the warm dust component is linked with  $f(\text{AGN})_{\text{MIR}}$ , and it also confirms that our threshold of  $f(\text{AGN})_{\text{MIR}} < 0.20$  for selecting SFGs is well founded. The middle panels are best interpreted in comparison with the bottom panels. When we examine the fraction of  $L_{\text{IR}}$  due to the cold dust component, we find that the Composites and SFGs have similar fractions ( $L_{\text{cold}}/L_{\text{IR}} \sim 0.52$ ), while the AGNs only have  $L_{\text{cold}}/L_{\text{IR}} \sim 0.25$ , despite having similar warm dust temperatures to the Composites.

Taken together, these data present a picture whereby the Composites are a true mix of the SFGs and AGNs. In SFGs, the warm dust arises from star-forming regions. Once an AGN significantly contributes to the mid-IR emission, warm dust heated by the AGN becomes more luminous than the warm dust located in star-forming regions, producing an increase in  $T_w$ . However, although a significant amount of the dust is now heated by a central AGN in the Composite galaxies, the cold dust emission still dominates  $L_{\text{IR}}$ . For the AGNs, a larger fraction of the dust mass is heated by the central AGN as indicated by the lower  $L_{\text{cold}}/L_{\text{IR}}$  ratios.

## 5. RELATION BETWEEN MID-IR AND FAR-IR

Throughout this paper, we have been discussing the AGN strength in the mid-IR. We now wish to explore how  $f(\text{AGN})_{\text{MIR}}$  correlates with the total contribution of the AGNs to  $L_{\text{IR}}$ . We use the three template libraries presented in Section 4 to calculate a conversion between  $f(\text{AGN})_{\text{MIR}}$  and  $f(\text{AGN})_{\text{total}}$ . First, we perform mid-IR spectral decomposition, described in Section 3.1, on each template from  $\lambda = 5\text{--}15\ \mu\text{m}$ . Next, we use a similar decomposition technique for the entire template. We fit simultaneously the  $z \sim 1$  star-forming SED and the Featureless AGN SED from Kirkpatrick et al. (2012). We removed the cold dust component from the Featureless AGN SED, as this component arises from the host galaxy. We have verified that the remaining SED does not contain any host emission using the decomposition package `DECOMPIR` presented in Mullaney et al. (2011). We modify the Featureless AGN SED with the extinction curve from Draine (2003), where we



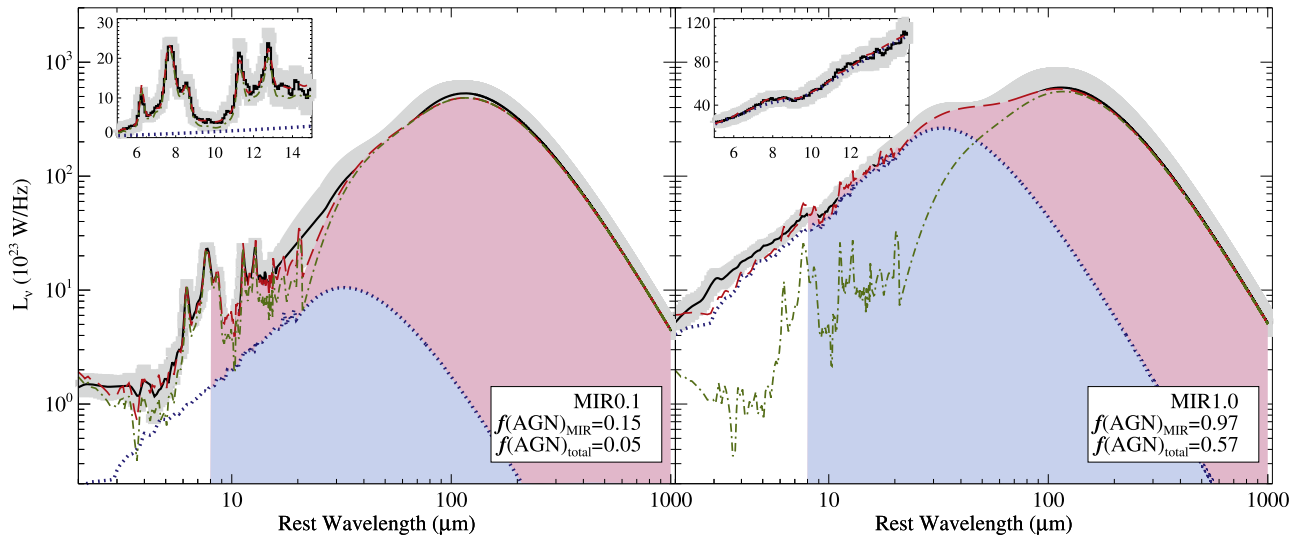


**Figure 13.** We illustrate our full IR decomposition technique for a star-forming template (MIR0.1, left) and an AGN template (MIR1.0, right). We find a best-fit model (red dashed line) by simultaneously fitting the  $z \sim 1$  star-forming SED (green dotted-dashed line) and Featureless AGN SED (blue dotted line), with extinction if required, from Kirkpatrick et al. (2012). We then integrate under the AGN component (blue dotted line) to calculate  $f(\text{AGN})_{\text{total}}$ , which is the fraction of  $L_{\text{IR}}$  (8–1000  $\mu\text{m}$ ) due to AGN heating. We have illustrated the integrated portion of the model and AGN component with the shaded regions. In the insets, we show the mid-IR decomposition (Equation (1)), used to calculate  $f(\text{AGN})_{\text{MIR}}$  from 5 to 15  $\mu\text{m}$ .

hold  $\tau$  fixed to the values derived from the mid-IR spectral decomposition. The normalizations of the AGN and star-forming SEDs are the only free parameters, and we allow them to vary simultaneously. Figure 13 illustrates two decomposition examples. We calculate  $f(\text{AGN})_{\text{total}}$  by integrating under the Featureless AGN SED to obtain the  $L_{\text{IR}}$  of the AGN component, and we express this as a fraction of the total  $L_{\text{IR}}$  (8–1000  $\mu\text{m}$ ). This simple decomposition technique works well for 80% of our templates. However, the Composite4, AGN1, AGN4, MIR6, COLOR4, and COLOR7 templates are not well fit, resulting in poor  $\chi^2$ , due to the cold dust peaking at significantly higher temperatures than the  $z \sim 1$  star-forming SED, and we exclude them from the analysis below.

We plot  $f(\text{AGN})_{\text{MIR}}$  versus  $f(\text{AGN})_{\text{total}}$  in Figure 14, where the filled symbols correspond to the template libraries. In the bottom panel, we quantify the relationship between  $f(\text{AGN})_{\text{MIR}}$  and  $f(\text{AGN})_{\text{total}}$  with a simple linear scaling (plotted as the dashed line)

$$f(\text{AGN})_{\text{total}} = (0.49 \pm 0.02) \times f(\text{AGN})_{\text{MIR}}, \quad (4)$$

where we have weighted each template by the number of sources comprising it. We require the linear fit to have a y-intercept of 0, so that  $f(\text{AGN})_{\text{total}} = 0$  when  $f(\text{AGN})_{\text{MIR}} = 0$ . The standard deviation around this relation is 9.6% (gray shaded region). Our composite templates lie below the dashed line while the AGNs lie above it, indicating that a simple linear scaling may not be the best choice, especially if  $f(\text{AGN})_{\text{MIR}}$  is well known.

In the top panel, we use a quadratic equation to quantify the relationship between  $f(\text{AGN})_{\text{MIR}}$  and  $f(\text{AGN})_{\text{total}}$ :

$$f(\text{AGN})_{\text{total}} = (0.66 \pm 0.09) \times f(\text{AGN})_{\text{MIR}}^2 - (0.035 \pm 0.07) \times f(\text{AGN})_{\text{MIR}}. \quad (5)$$

Again, we have weighted each template by the number of sources that comprise it, and we have forced the y-intercept to be 0. We plot this relationship, and the corresponding standard deviation of 5.8%, as the dark dashed line and gray shaded

region, respectively. The smaller standard deviation indicates that this is a better fit for our templates.

We independently test the validity of our relation using the SEDs of individual sources with exceptional photometric coverage of the far-IR. We have already decomposed the mid-IR spectra of these sources, and we decompose the full SEDs using the same procedure as for our templates. We plot these sources as the black crosses. The scatter among the individual sources better illustrates the uncertainty associated with our decomposition methods, but in general, the trend between  $f(\text{AGN})_{\text{MIR}}$  and  $f(\text{AGN})_{\text{total}}$  for the sources agrees remarkably well with the templates and reinforces that the quadratic relation is a better fit to the data than the linear scaling.

The quadratic relation arises because AGN-heated dust emission falls off sharply after 40  $\mu\text{m}$ , so  $L_{\text{IR}}$  is dominated by stellar heating after this wavelength. That is, until the AGN boosts the warm and hot dust emission enough to outshine the cold diffuse dust, which Figure 7 indicates happens when  $f(\text{AGN})_{\text{MIR}} > 0.70$ . This nonlinear relationship supports what we found earlier, i.e., that composites are an intermediate class between SFGs and AGNs where most of the far-IR emission can be attributed to star formation, although the AGN is dominating at shorter wavelengths.

Since we have determined  $f(\text{AGN})_{\text{total}}$ , we can scale  $L_{\text{IR}}$  by  $(1 - f(\text{AGN})_{\text{total}})$  to obtain  $L_{\text{IR}}^{\text{SF}}$ , the portion of  $L_{\text{IR}}$  due only to heating by stellar radiation (listed in Table 3). We could not decompose the full IR SED of the Composite4, AGN1, AGN4, MIR6, COLOR4, and COLOR7 templates, so we calculate  $f(\text{AGN})_{\text{total}}$  using Equation (5).  $L_{\text{IR}}^{\text{SF}}$  is a crucial quantity for obtaining accurate SFRs. In future surveys, particularly with *JWST*,  $f(\text{AGN})_{\text{MIR}}$  can be determined using mid-IR spectroscopy; this can then be converted into  $f(\text{AGN})_{\text{total}}$  using one of our relations, and  $L_{\text{IR}}$  can be scaled accordingly so as not to overestimate SFRs. Carefully removing the AGN contribution to  $L_{\text{IR}}$  will provide a more accurate understanding of the build-up of stellar mass in the early universe.

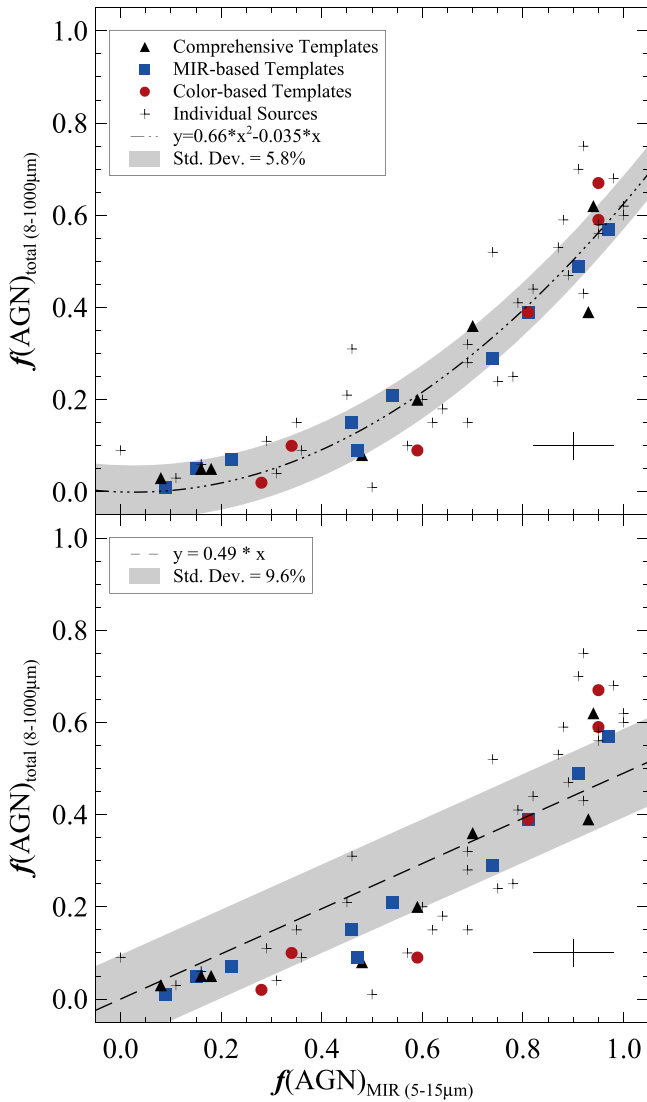


**Figure 14.**  $f(\text{AGN})_{\text{MIR}}$  vs.  $f(\text{AGN})_{\text{total}}$ . Typical uncertainties on each parameter are shown in the lower right corner.  $f(\text{AGN})_{\text{MIR}}$  has a higher error because we have included an extinction component in this fit, while when fitting  $f(\text{AGN})_{\text{total}}$ , we only allow the relative normalizations to vary. We fit a quadratic equation (top panel) and a linear relation (bottom panel) to our templates (filled symbols). The standard deviation of the templates around each relation is shown as the gray shaded region. We have a handful of sources ( $\sim 30$ ) with exceptionally well-sampled SEDs, allowing us to decompose the entire SED into an AGN component and a star-forming component. We plot these sources as the crosses. They are not included in the linear or quadratic fits or the calculations of standard deviation, but they agree remarkably well with these relations, ensuring the reliability of our results. The quadratic relation provides a better fit to the data.

Finally, we wish to comment on how our far-IR properties relate to another commonly used measure,  $L(\text{FIR})$ , which is the integrated luminosity from 50 to 300  $\mu\text{m}$ .  $L_{\text{cold}}$  accounts for most of the emission in this wavelength regime, and we find a nearly linear relationship between  $L_{\text{cold}}$  and  $L(\text{FIR})$ :

$$L(\text{FIR}) = 6.92 L_{\text{cold}}^{0.94} \quad (6)$$

$L_{\text{cold}}$  also accounts for the bulk of  $L_{\text{IR}}$  attributed to star formation by our decomposition technique, and  $L_{\text{cold}}$  and  $L_{\text{IR}}^{\text{SF}}$  have a nearly linear relationship as well:

$$L_{\text{IR}}^{\text{SF}} = 9.31 L_{\text{cold}}^{0.94} \quad (7)$$

The strong correlation between  $L(\text{FIR})$  and  $L_{\text{IR}}^{\text{SF}}$  strengthens our conclusion that heating by star formation accounts for the bulk of the cold, far-IR emission.

## 6. DISCUSSION

### 6.1. Consistency in SFGs over Cosmic Time

We have carefully decomposed the mid-IR spectra of our sources, allowing us to classify galaxies harboring a buried AGN that may not be visible at other wavelengths. An additional benefit of this classification scheme is that it enables us to isolate the mid- and far-IR properties of purely SFGs over a large range in redshift. Within the Comprehensive Library, we have determined the average SEDs of pure SFGs with median redshifts of  $z \sim 0.8$  and  $z \sim 1.7$ , and these templates are indistinguishable (left column of Figure 11). In particular, we find that mid-IR classification is an excellent predictor of far-IR emission, and this is not a trivial result since mid-IR and far-IR emission are tracing different dust populations at different spatial locations.

Before we discuss the full IR SED, we want to comment on our mid-IR identification technique. Our technique for selecting SFGs hinges on the PAH emission, and it is possible that we could misidentify SFGs that have mid-IR emission dominated by star formation, but also have weak PAH emission. However, based on previous results in the literature, we do not think these types of galaxies are common in samples of (U)LIRGs; locally, such galaxies are low-metallicity dwarfs (e.g., Wu et al. 2006). The similarity of PAH emission among SFGs is also seen in Battist et al. (2015), which compares PAH features of local SFGs ( $L_{\text{IR}} \sim 10^{10} L_{\odot}$ ) and finds remarkable consistency. These galaxies have been classified as SFGs according to optical emission line ratios. Battist et al. (2015) also compares the average PAH emission of these local SFGs with the star-forming templates from Kirkpatrick et al. (2012) and finds they are consistent, showing no evolution of PAH emission features with redshift or luminosity. Petric et al. (2011) classifies local (U)LIRGs from the Great Observatories All Sky Survey (GOALS; Armus et al. 2009) as SFGs based on mid-IR flux ratios and finds that PAH emission in all SFGs is qualitatively similar. On the other hand, Polletta et al. (2008) and Bauer et al. (2010) conclude that the mid-IR continuum in high-redshift ULIRGs with weak PAH features is dominated by quasar emission, although these sources can still have a significant amount of  $L_{\text{IR}}$  due to star formation. Our results are consistent with these previous studies.

Our SFG templates have no significant change in  $T_w$ ,  $T_c$ , or  $L_{\text{cold}}/L_{\text{IR}}$  with redshift or  $L_{\text{IR}}$ , effectively demonstrating that the average dust heating in SFGs remains constant over a broad epoch. This result does not contradict observations from Béthermin et al. (2015). For a sample of main-sequence galaxies spanning a redshift range of  $z = 0.5$ –4, the authors conclude that the average interstellar radiation field, measured by the parameter  $\langle U \rangle$ , increases as  $\langle U \rangle \propto (1 + z)^{1.15}$ .  $\langle U \rangle$  is proportional to dust temperature, indicating that the dust temperature should be increasing and the peak of the SED should be shifting to shorter wavelengths. However, when we plot the stacked detections in Béthermin et al. (2015) in the same redshift range as our templates ( $0.25 < z < 1.25$  and  $1.25 < z < 2.00$ ), we find that the stacked fluxes are consistent with our SEDs within the uncertainties. The evolution in SED peak observed in Béthermin et al. (2015) is not strong enough

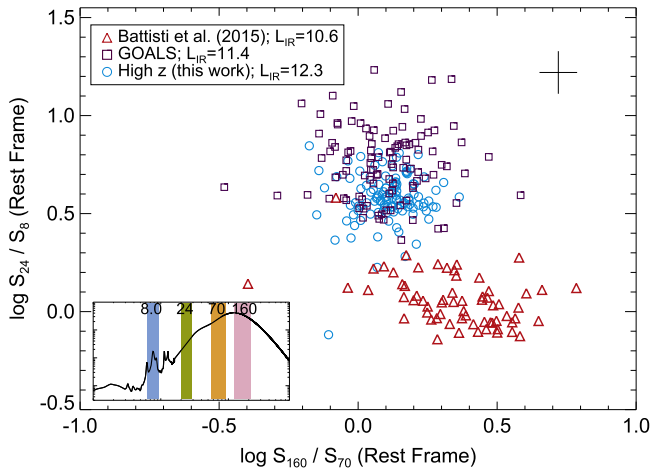


**Figure 15.** We plot the colors  $S_{160}/S_{70}$  (rest frame) and  $S_{24}/S_8$  (rest frame) of three samples: local star-forming LIRGs from GOALS (purple squares), local normal SFGs (red triangles), and our SFGs (blue circles). The median  $L_{\text{IR}}$  of each sample is listed in the legend. We have estimated the rest-frame colors for our SFGs by sampling the MIR0.0–MIR0.2 templates within the template uncertainties. Average uncertainties produced by this method are illustrated by the cross in the upper right corner. Our high- $z$  SFGs show a strong overlap with the GOALS LIRGs, but the less luminous local SFGs lie in a different region of colorspace. This indicates that the SEDs of local LIRGs are similar to the SEDs of high- $z$  LIRGs and ULIRGs.

to be evident over the redshift range we are probing, which is more limited than that study.

Our observed lack of SED evolution is consistent with observations of the larger sample of GOODS-*Herschel* SFGs; the ratio of PAH to far-IR emission, as traced by  $L_{8\mu\text{m}}/L_{\text{IR}}$ , is constant from  $z = 0$ –2.5, providing evidence that the IR SEDs of normal, non-interacting, dusty SFGs do not evolve strongly (Elbaz et al. 2011). In contrast, local ULIRGs have a deficit of PAH emission compared with less luminous, normal SFGs (e.g., Veilleux et al. 2009). However, at higher redshift, this deficit is seen to shift to higher  $L_{\text{IR}}$ , so that high-redshift ULIRGs have  $L_{\text{PAH}}/L_{\text{IR}}$  ratios that mimic local LIRGs, indicating that local LIRGs might be an ideal comparison sample for our high-redshift LIRGs and ULIRGs (Sajina et al. 2012; Pope et al. 2013; Stierwalt et al. 2013).

We compare the IR colors of our high- $z$  SFG sources with the observed-frame IR colors of local LIRGs in Figure 15. We plot  $S_{160}/S_{70}$  and  $S_{24}/S_8$  for LIRGs from GOALS. The individual galaxies in GOALS all have mid-IR spectroscopy available, allowing us to classify their mid-IR AGN emission using the same technique as for our high-redshift galaxies. In Figure 15, we are only comparing mid-IR identified SFGs ( $f(\text{AGN})_{\text{MIR}} < 0.2$ ) in the GOALS and high- $z$  samples. For the high- $z$  sources, we have estimated rest-frame  $S_{160}/S_{70}$  and  $S_{24}/S_8$  colors using a Monte Carlo technique to sample the MIR0.0, MIR0.1, and MIR0.2 templates within the template uncertainties at 8, 24, 70, and 160  $\mu\text{m}$ . We show the typical uncertainty on this synthetic photometry in the upper right corner. We also demonstrate the portion of the SED traced by these colors in the lower left corner.

There is a strong overlap between our high- $z$  SFGs and the GOALS SFGs. For comparison, we plot local less luminous ( $L_{\text{IR}} \sim 10^9$ – $10^{10}$ ) SFGs identified through optical emission line ratios (O’Dowd et al. 2011; Battistini et al. 2015). Although a few of these sources lie in the same region as GOALS and our SFGs, in general these sources lie below and to the right of the

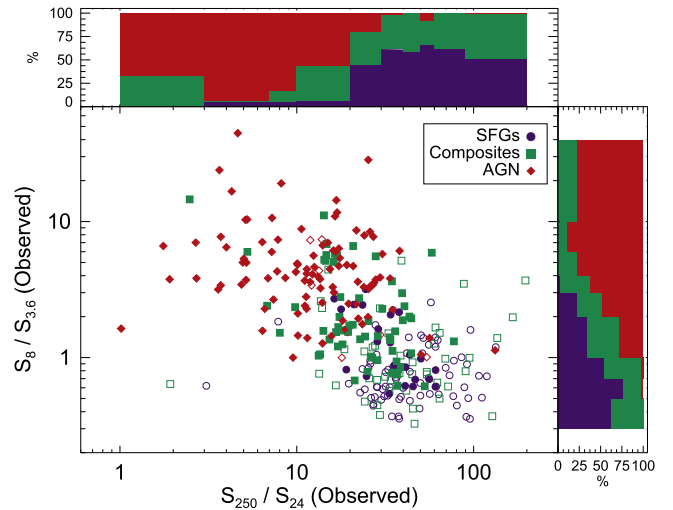


**Figure 16.** Our sources in colorspace. We shade the sources according to their mid-IR power source. SFGs (blue circles) have  $f(\text{AGN})_{\text{MIR}} < 0.2$ , composites (green squares) have  $f(\text{AGN})_{\text{MIR}} = 0.2$ –0.8, and AGNs (red diamonds) have  $f(\text{AGN})_{\text{MIR}} > 0.9$ . The full sample is plotted with the open symbols while sources with  $S_{24} > 0.9$  mJy are plotted with the filled symbols. To the top and right, we plot the color demographics of our sources, where we have corrected for completeness effects by weighting the distributions by the 24  $\mu\text{m}$  number counts presented in Béthermin et al. (2010). These distributions are useful for estimating relative numbers of SFGs and AGNs when only a couple of photometric data points exist for each source.

more luminous galaxies.  $S_{160}/S_{70}$  traces the peak of the SED, while  $S_{24}/S_8$  traces the amount of warm dust relative to the PAH emission. That we see little difference in either of these colors between the GOALS and high- $z$  SFGs indicates that the average SED of high-redshift LIRGs and ULIRGs is remarkably similar to local LIRGs. In other words, the SEDs of luminous dusty galaxies may not evolve strongly with redshift, if we do not consider the extreme cases of compact mergers. This result agrees with Stierwalt et al. (2013), where the authors compared the average mid-IR spectra of the GOALS LIRGs with the average mid-IR spectra of submillimeter galaxies (SMGs) from Menéndez-Delmestre et al. (2009). Stierwalt et al. (2013) find that when all mid-IR AGN contribution is removed, the remaining spectra of local star-forming LIRGs are identical to those of high- $z$  star-forming SMGs. We will explore more comparisons between the GOALS survey and our high-redshift sources in a future work (A. Kirkpatrick et al. 2016, in preparation).

## 6.2. Demographics in Color Space

Our templates represent the average SEDs of our sample, but the variation among sources in the sample can be seen in Figure 16, where we again plot the colors  $S_{250}/S_{24}$  and  $S_8/S_{3.6}$  for our sample. We shade the sources according to  $f(\text{AGN})_{\text{MIR}}$ , so that SFGs (blue circles) have  $f(\text{AGN})_{\text{MIR}} < 0.2$ , composites (green squares) have  $f(\text{AGN})_{\text{MIR}} = 0.2$ –0.8, and AGNs (red diamonds) have  $f(\text{AGN})_{\text{MIR}} > 0.8$ . Our sample comprises 24  $\mu\text{m}$  faint galaxies from GOODS and 24  $\mu\text{m}$  bright galaxies, primarily from xFLS. We illustrate the difference in these samples using filled and unfilled symbols. The filled symbols all have  $S_{24} > 0.9$  mJy, and primarily lie to the upper left. AGNs and SFGs lie in distinct regions in this colorspace, with AGNs occupying primarily the upper left quadrant.



**Table 5**  
Color Distributions

Min Color	Max Color	SFG	Composite	AGN
$S_8/S_{3.6}$				
0.3	0.5	62.1	37.9	0.0
0.5	0.7	76.8	21.3	1.8
0.7	1.0	54.5	42.9	2.6
1.0	2.0	34.7	37.4	27.9
2.0	3.0	21.9	30.2	47.8
3.0	4.0	2.2	36.0	61.8
4.0	6.0	0.0	22.9	77.1
6.0	10.0	0.0	11.4	88.6
10.0	70.0	0.0	22.6	77.4
$S_{250}/S_{24}$				
1.0	3.0	0.0	33.1	66.9
3.0	7.0	4.6	1.9	93.5
7.0	10.0	5.4	11.4	83.2
10.0	20.0	6.4	37.0	56.6
20.0	30.0	45.2	34.7	20.1
30.0	40.0	61.6	36.3	2.1
40.0	50.0	58.6	41.4	0.0
50.0	60.0	65.7	26.3	8.0
60.0	90.0	62.5	37.5	0.0
90.0	200.0	50.9	48.5	0.6

**Note.** We list the percentages of SFGs, Composites, and AGNs in each color bin shown in Figure 16.

Because we are combining sources selected at different  $S_{24}$  thresholds, we do not have a complete sample. We account for completeness using the  $24\ \mu\text{m}$  number counts from Béthermin et al. (2010). The authors list the number counts in  $24\ \mu\text{m}$  flux bins from  $S_{24} = 0.035$ – $100\ \text{mJy}$ . We divide our sources into the same flux bins, and assign a weight to each source, so that our weighted number counts match what is presented in Béthermin et al. (2010). We then divide the colors  $S_8/S_{3.6}$  and  $S_{250}/S_{24}$  into refined bins and count the weighted number of sources in each bin to produce the color demographic histograms on the top and right of Figure 16. We list the color bins and weighted percentages of SFGs, composites, and AGNs in each bin in Table 5. The composites are roughly equally distributed. This is because of variable levels of AGNs within the composites but may also be linked to different triggering mechanisms for an AGN growth. Major mergers are known to produce warmer SEDs, but an AGN growing in a clumpy, extended disk likely has more cold dust (Elbaz et al. 2011). AGNs and SFGs separate cleanly in both  $S_8/S_{3.6}$  and  $S_{250}/S_{24}$ , making each of these colors advantageous for selecting AGNs and SFGs in a sample lacking spectroscopy or broad photometric coverage of the SED.

We illustrate how our color demographics can be applied to large samples, to estimate the number of pure SFGs for example, using a catalog of 10,300 *BzK* galaxies with a detection in  $S_8$  and  $S_{3.6}$  (Lin et al. 2012). We first determine the  $S_8/S_{3.6}$  distribution of *BzKs* using the bins listed in Table 5. Then, we multiply the number of *BzKs* in each bin by the respective percentages of SFGs in Table 5 to estimate the number of *BzKs* that are SFGs. We calculate from the full *BzK* catalog that only 23% are pure SFGs. This could have implications for studies that see a redshift evolution in the shape of the SED. For example, using the same *BzK* catalog,

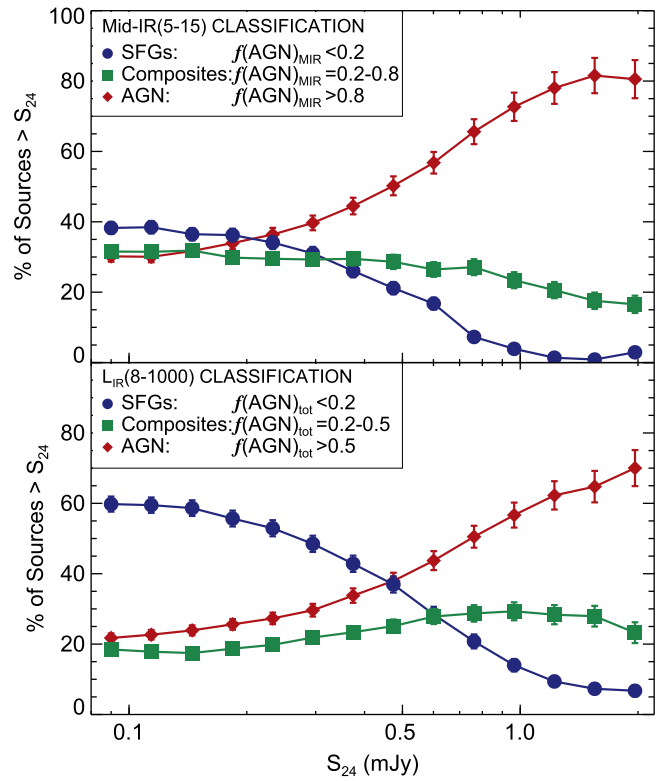


**Figure 17.** We present the cumulative  $S_{24}$  distribution of our sample. In the top panel, we classify sources as SFG, composite, or AGN based on  $f(\text{AGN})_{\text{MIR}}$ . In the bottom panel, we calculate  $f(\text{AGN})_{\text{total}}$  using Equation (5) and then sort sources accordingly. Each point represents the percentage of SFGs, composites, or AGNs brighter than a given  $24\ \mu\text{m}$  flux. We have assigned weights to each galaxy based on its  $24\ \mu\text{m}$  flux density in order to reproduce the number counts presented in Béthermin et al. (2010). The cumulative distribution presented here is calculated using our sources' weights. We have attached Poisson errors to each point. AGNs dominate at brighter fluxes. Composites contribute 20%–30% at all flux thresholds in both panels, illustrating the necessity of properly estimating or removing composites from IR samples of SFGs.

Magdis et al. (2012) measure  $\langle U \rangle \propto (1+z)^{1.15}$  from  $z=0$ – $2$ , where  $U \propto T_c$ . The authors have removed X-ray-luminous AGNs, but according to our  $S_8/S_{3.6}$  color diagnostic, it is possible that many composites hosting an obscured AGN are included in their sample. We find a similar evolution of dust temperature with redshift for our Composites templates, but this is noticeably absent for our SFG templates (Figure 12). Our color demographics can help estimate the level of contamination in a large sample from galaxies that possess a mix of star formation and AGN activity. Our composites may be missed at X-ray wavelengths due to either high column densities or lower AGN X-ray luminosities. Moreover, the optical line ratios expected in composites are currently unconstrained at high redshift (Kartaltepe et al. 2015). Our IR color technique then provides a unique opportunity to identify the AGNs lurking in dusty, IR-luminous galaxies.

In Figure 17, we examine the effect that  $24\ \mu\text{m}$  flux thresholds can have on the number of composites, SFGs, and AGNs in a given sample. Again, we use the number count weights assigned to our sources, and plot the percentages of SFGs, composites, and AGNs brighter than a given  $24\ \mu\text{m}$  flux threshold (top panel). Throughout this paper, we have discussed SFGs, composites, and AGNs using a mid-IR classification scheme, but in the bottom panel of Figure 17, we classify sources according to  $f(\text{AGN})_{\text{total}}$ . Here, we have

calculated  $f(\text{AGN})_{\text{total}}$  for all sources using Equation (5). SFGs have  $f(\text{AGN})_{\text{total}} < 0.2$ , composites have  $f(\text{AGN})_{\text{total}} = 0.2\text{--}0.5$ , and AGNs have  $f(\text{AGN})_{\text{total}} > 0.5$ , a threshold chosen because  $L_{\text{IR}}$  is now dominated by AGN emission. Although  $f(\text{AGN})_{\text{total}}$  is derived from  $f(\text{AGN})_{\text{MIR}}$ , we stress that the IR classifications are not the same as the mid-IR classifications. Both panels of Figure 17 show that AGNs dominate at brighter fluxes ( $S_{24} > 0.5$  mJy), so imposing a simple flux cut on a sample can easily remove large numbers of AGNs. IR SFGs dominate the population when  $S_{24} < 0.4$  mJy (bottom panel), but mid-IR SFGs never do (top panel). However, IR and mid-IR composite sources contribute about 20%–30% of a sample at all  $S_{24}$  thresholds, so simply removing IR-bright AGNs or X-ray AGNs does not account for all IR AGN emission.

These demographics are useful for current and future high-redshift studies, particularly with *JWST*. The MIRI instrument on *JWST* will have a broadband  $25.5\text{ }\mu\text{m}$  filter, so the  $S_{24}$  distributions in Figure 17 can inform desired sensitivities of a particular project. Contamination by obscured AGN emission needs to be accounted for since Figure 17 demonstrates that AGNs and composites are non-negligible at all  $S_{24}$  thresholds. Through MIRI and NIRC2, astronomers will also be able to obtain a color very similar to  $S_8/S_{3.6}$ , and so our color demographic in Figure 16 and Table 5 can be used to estimate the number of SFGs and AGNs in a given sample or select galaxies for further study.

## 7. SUMMARY

We have decomposed mid-IR spectroscopy to robustly determine the strength of an AGN, classified as the fraction of mid-IR luminosity due to power-law continuum emission, in a sample of 343 high-redshift (U)LIRGs. We define three general classifications: SFGs ( $f(\text{AGN})_{\text{MIR}} < 0.2$ ), composites ( $f(\text{AGN})_{\text{MIR}} = 0.2\text{--}0.8$ ), and AGNs ( $f(\text{AGN})_{\text{MIR}} > 0.8$ ). Based on these mid-IR classifications, we have created three publicly available template libraries designed for use with high-redshift LIRGs and ULIRGs. The appropriate library depends on the data available to the user.

1. MIR-based Library. This is ideal if information about the mid-IR power source is available, but few far-IR data are available.
2. Color-based Library. These are ideal for high-redshift sources that only have photometric data available.
3. Comprehensive Library. This library is based on comprehensive intrinsic galaxy information. We have used it to study dust emission trends with  $f(\text{AGN})_{\text{MIR}}$ , redshift, and  $L_{\text{IR}}$ . Choosing the appropriate template from this library requires knowledge about a source's  $L_{\text{IR}}$  and redshift.

Using our empirical templates, we find the following.

1. SFGs are remarkably similar from  $z \sim 0.3\text{--}2.8$ . The shape of the mid-IR and far-IR emission is nearly identical for the three SFG templates from the Comprehensive Library, and the dust temperatures ( $T_c$ ,  $T_w$ ) and normalizations ( $L_{\text{cold}}/L_{\text{IR}}$ ) are consistent. Furthermore, the colors of these templates are similar to colors of low-redshift LIRGs from GOALS, indicating that local analogs exist for high-redshift star-forming LIRGs and ULIRGs, albeit at a slightly lower  $L_{\text{IR}}$ . A detailed

- comparison of the dust emission of high-redshift (U)LIRGs and their local analogs will be discussed in an upcoming study (Kirkpatrick et al. 2016, in preparation).
2. For composites and AGNs, the cold dust temperature,  $T_c$ , changes with  $L_{\text{IR}}$  and redshift, but it is not affected by the strength of the AGN as  $T_c$  arises from the host galaxy.
3. The warm dust temperature,  $T_w$ , and the relative amount of cold dust emission,  $L_{\text{cold}}/L_{\text{IR}}$ , are strong functions of  $f(\text{AGN})_{\text{MIR}}$ . As the AGN grows more luminous, it heats more of the dust to higher temperatures, eventually outshining the cold dust component.  $f(\text{AGN})_{\text{MIR}} = 0.6$  is an interesting threshold where  $T_w$  peaks and  $L_{\text{cold}}/L_{\text{IR}}$  begins to decline.
4.  $f(\text{AGN})_{\text{MIR}}$  is related to the total amount of  $L_{\text{IR}}$  from AGN heating,  $f(\text{AGN})_{\text{total}}$ , by a second-degree polynomial. Due to the quadratic nature of the relationship, an AGN does not significantly contribute to  $L_{\text{IR}}$  until  $f(\text{AGN})_{\text{MIR}} > 0.6$ .  $f(\text{AGN})_{\text{total}}$  is useful to correct the amount of  $L_{\text{IR}}$  attributable to star formation and obtain more accurate SFRs.
5. In general, we find that composites are a true mix of SFGs and AGNs, and may represent a transition between the two. A merger or other instability triggers the growth of an AGN, which can heat the dust below  $\sim 40\text{ }\mu\text{m}$  and suppress PAH emission, producing higher  $f(\text{AGN})_{\text{MIR}}$  values. However, the AGN does not manifest itself on the far-IR emission until  $f(\text{AGN})_{\text{MIR}} > 0.6$ , and eventually the AGN-heated dust outshines the diffuse dust.
6. We estimate how prevalent AGNs and composites are at different  $24\text{ }\mu\text{m}$  selection thresholds, and find that  $>40\%$  of a sample selected at  $S_{24} > 0.1$  mJy may be hosting a buried AGN. Composites and AGNs have at least  $>20\%$  of  $L_{\text{IR}}$  due to AGN heating, illustrating the necessity of accounting for AGN heating when studying dust emission or IR-based SFRs at high redshift.

Our infrared analysis will be applicable for forthcoming data from *JWST*. MIRI will provide medium-resolution spectroscopy from  $5$  to  $28\text{ }\mu\text{m}$ . Our spectral decomposition technique requires coverage of the PAH complexes from  $6$  to  $13\text{ }\mu\text{m}$ . With the coverage of MIRI, our mid-IR decomposition technique can be used to identify mid-IR AGNs out to  $z \sim 2$ . We have also demonstrated that the color  $S_8/S_{3.6}$ , obtainable with *JWST*, can be used to separate AGNs from SFGs in the range  $z = 0\text{--}2.8$ . Future observations with *JWST* can reach deeper  $24\text{ }\mu\text{m}$  limits to determine the prevalence of AGNs and composites in these samples.

We thank the anonymous referee for thoughtful comments that have helped to improve the clarity and impact of this work. We acknowledge support from NSF AAG grants AST-1312418 and AST-1313206. S.S. also gratefully acknowledges support from the L'Oreal USA For Women in Science program. T.D. acknowledges support from ALMA-CONICYT project 31130005 and FONDECYT project 1151239.

## APPENDIX A ALTERNATIVE FITTING METHODS

We fit the far-IR SED with an optically thin 2T MBB to construct our templates, and we now discuss whether this fitting method is optimal for determining dust temperatures and

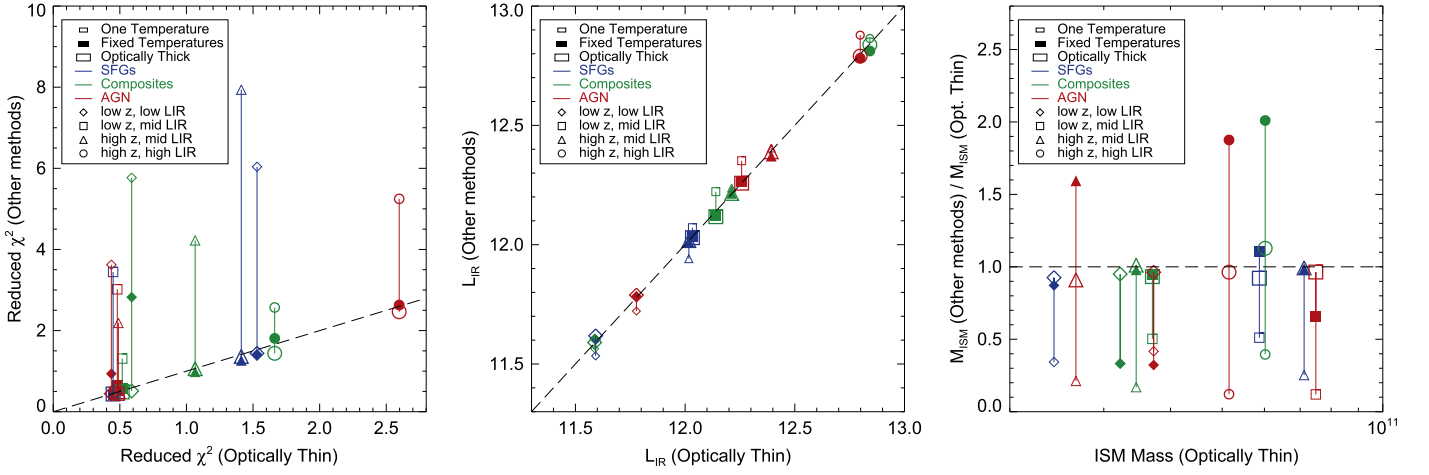


**Figure 18.** Left Panel—comparison of the reduced  $\chi^2$  values from our different fitting methods. Colors and symbols correspond to each template from the Comprehensive Library. Filled symbols are the reduced  $\chi^2$  values derived when the two temperature components are held fixed; large open symbols are derived using the optically thick assumption; small open symbols are derived with only a one-temperature MBB, instead of two temperatures. We overplot a one-to-one relation as the dashed line. The 1T MBB method produces the worst reduced  $\chi^2$  values, while there is a smaller difference between the reduced  $\chi^2$  values using the optically thick or optically thin dust assumption. Middle panel—we compare the  $L_{\text{IR}}$  values calculated from each method.  $L_{\text{IR}}$  is essentially independent of the particular far-IR fitting method. Right panel—we compare the ISM masses derived from each fitting method. The optically thick and optically thin assumptions produce consistent ISM masses, while the one-temperature fitting method results in significantly lower ISM masses.

$L_{\text{IR}}$ . We use the subsamples in the Comprehensive Library to explore three alternative fitting methods:

1. Optically thick dust;
2. Fixed dust temperatures;
3. One-temperature MBB.

For each method, we follow the same fitting procedure outlined in Section 4, and we compare the results with the optically thin 2T MBB fits used to create our templates. We quantify the goodness of the fits with the reduced  $\chi^2$  statistic, and we compare the reduced  $\chi^2$  values in the left panel of Figure 18.

$L_{\text{IR}}$  is typically a desired quantity when fitting far-IR data. We compare  $L_{\text{IR}}$  calculated from each of the three alternative fitting methods with our template  $L_{\text{IR}}$ s (Table 3) in the middle panel of Figure 18. We find no significant difference for any of the templates, showing that  $L_{\text{IR}}$  is robust against these particular fitting methods. However,  $L_{\text{IR}}$  is not the only useful parameter that can be derived from fitting far-IR photometry with a model; another commonly calculated quantity is ISM mass. We demonstrate how a particular far-IR fitting technique affects the derived ISM mass in the right panel of Figure 18. For each template, we calculate the ISM mass at 850  $\mu\text{m}$ , which is in the Rayleigh–Jeans tail of the dust emission and is a more reliable tracer of the ISM mass (Scoville et al. 2014). We use the following equation:

$$M_{\text{ISM}} = \frac{\lambda^2 L_\nu}{8\pi k \kappa_{\text{ISM}} T_c}. \quad (8)$$

$\kappa_{\text{ISM}}$  is the dust opacity per grain and is related to the opacity  $\tau_\nu$ .  $\tau_{250}/N_{\text{H}}$  has been recently measured by the Planck Collaboration (2011), and from that value, Scoville et al. (2014) calculate  $\kappa_{\text{ISM}}(\nu_{250})$ :

$$\kappa_{\text{ISM}}(\nu_{250}) = \frac{\tau_{250}}{N_{\text{H}} 1.36 m_{\text{H}}} \quad (9)$$

where  $N_{\text{H}}$  is the column density of hydrogen.  $\kappa_{\text{ISM}}(\nu_{250})$  can then be scaled to 850  $\mu\text{m}$ :

$$\kappa_{\text{ISM}}(\nu_{850}) = \kappa_{\text{ISM}}(\nu_{250}) \times \left(\frac{250}{850}\right)^{-\beta}. \quad (10)$$

### A.1. Optically Thick Dust

The optically thin dust approximation is commonly adopted with a limited number of data points, but it might not be an accurate assumption at  $\lambda \ll 100 \mu\text{m}$ , particularly in starbursts. We test what effect using the full optically thick equation has on the dust temperatures by fitting to the far-IR data points of each template in the Comprehensive Library. We fit

$$S_\nu = a_1 \times (1 - e^{-\tau(\nu)}) \times B_\nu(T_{\text{warm}}) + a_2 \times (1 - e^{-\tau(\nu)}) \times B_\nu(T_{\text{cold}}), \quad (11)$$

where  $\tau(\nu) = (\nu/\nu_0)^\beta$ . We use  $\beta = 1.5$ , and we assume  $\nu_0 = 300 \text{ GHz}$  ( $\lambda_0 = 100 \mu\text{m}$ ). The optically thick equation produces reduced  $\chi^2$  values consistent with the optically thin fitting. As for the physical parameters, we find that the optically thick equation has a negligible effect on  $T_c$  and  $L_{\text{cold}}/L_{\text{IR}}$ , since the cold dust is presumably optically thin, but increases the derived  $T_w$  by  $\sim 20 \text{ K}$ . However, the exact value of  $T_w$  ultimately has little effect on  $L_{\text{IR}}$ , and the warm dust component accounts for  $\sim 1\%$  of the ISM mass. Since  $\chi^2$ ,  $L_{\text{IR}}$ , and  $M_{\text{ISM}}$  do not change significantly when assuming optically thin dust, we recommend using the optically thin approximation for simplicity.

### A.2. Fixed Dust Temperature

We experiment with holding the dust temperatures fixed, which is another useful technique when limited data are available. We hold the temperatures fixed to the average  $T_c$  and  $T_w$  values for the SFGs, Composites, and AGNs, separately. In

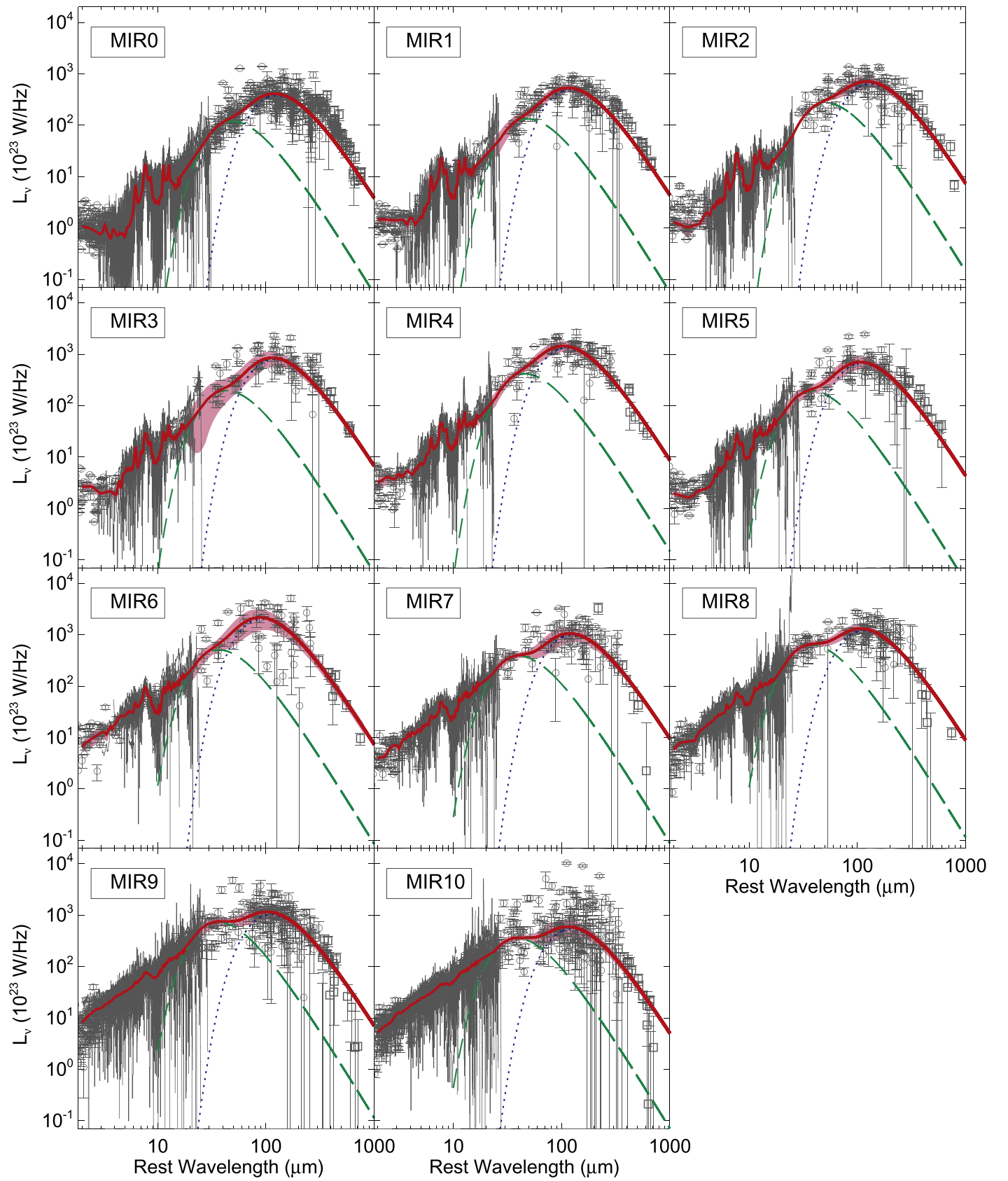


Figure 19. MIR-based Library.



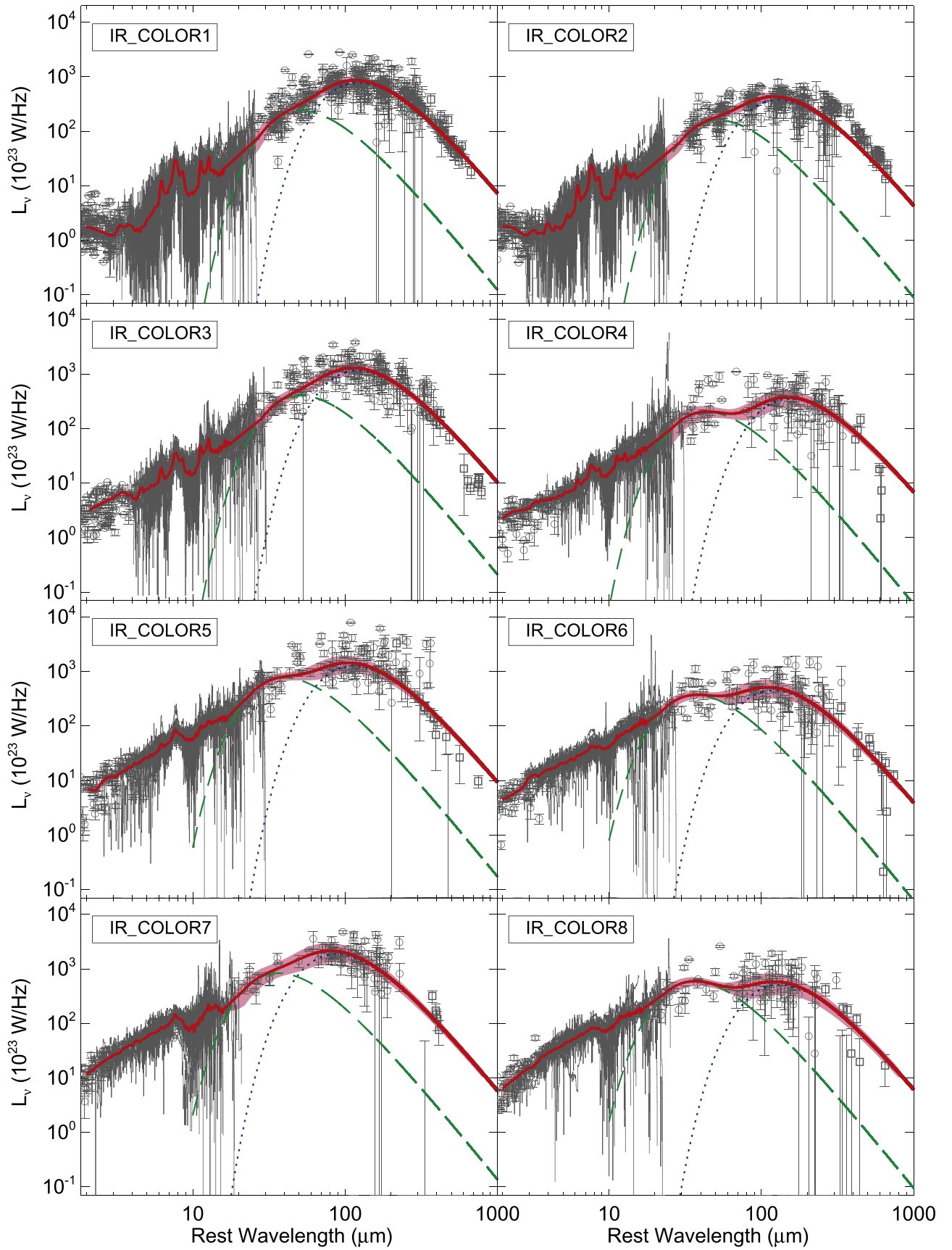


Figure 20. Color-based Library.

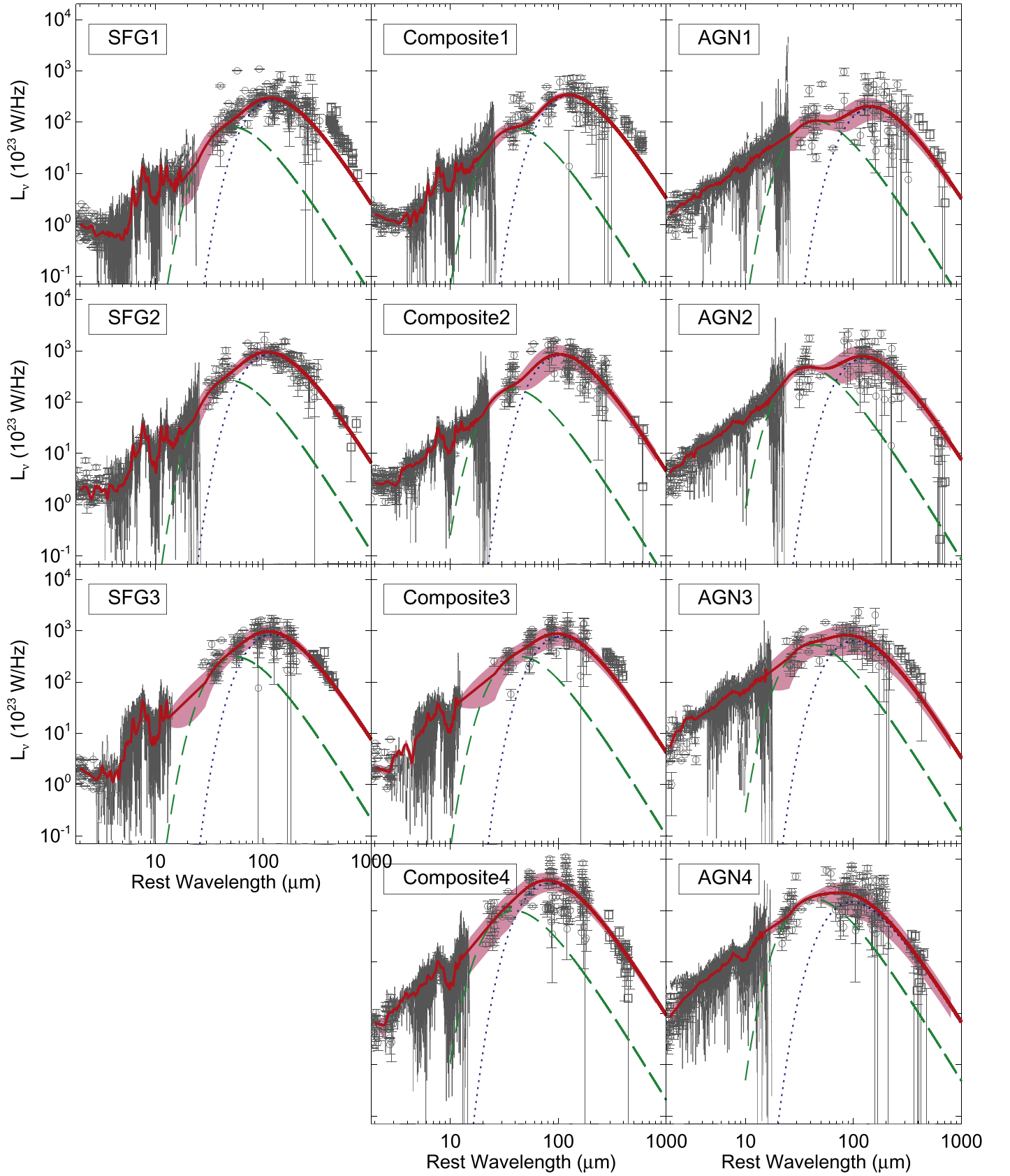


Figure 21. Comprehensive Library.

general, holding the temperatures fixed has little effect on the relative normalizations of the dust component, so the ratio  $L_{\text{cold}}/L_{\text{IR}}$  is approximately constant compared with when the

dust temperatures are allowed to vary.  $M_{\text{ISM}}$  is significantly higher for the Composite4, AGN3, and AGN4 templates, and lower for the AGN1 and AGN2 templates. The AGN templates

show the largest increase of  $T_c$  with  $L_{\text{IR}}$  and redshift, and this is not captured by holding the temperatures fixed, producing incongruous ISM masses.

We also attempt to fit a 3T MBB, as this may be more physically appropriate, particularly for the AGN sources. In this case, the coldest dust component comes from the diffuse ISM, a warmer component is due to heating from star-forming regions, and a hot component is due to heating by an AGN. In order to achieve good fits, we had to assume dust temperatures. Based on the temperatures of the diffuse component and star-forming regions in the local universe, we assumed  $T_c = 20$  K,  $T_w = 40$  K, and  $T_h = 100$  K (e.g., Clemens et al. 2013). The results produced good reduced  $\chi^2$  fits and consistent  $L_{\text{IR}}$ s, but we do not advocate this technique as it requires assumptions about the dust temperatures that may not hold at high redshift.

### A.3. One Temperature

Finally, we test how good a fit we can achieve with only a 1T MBB, which is commonly adopted in the literature due to incomplete photometric coverage of the far-IR. In this case, the reduced  $\chi^2$  values are typically poor ( $>2$ ). This result occurs because we are fitting the wavelength range  $\lambda \sim 20\text{--}300\ \mu\text{m}$ , and a 1T MBB will necessarily be biased to higher dust temperatures by including this much data. The 1T MBB produces consistently lower ISM masses, typically 60%–70% lower than the optically thin 2T MBB method, due to both the difference in  $T_c$  and the extrapolated  $L_{850}$ . If only SPIRE data are available, we recommend adding in a warm dust component with a fixed temperature in order to ensure that the cold dust temperature is not biased to warmer wavelengths (e.g., Kirkpatrick et al. 2014a). A 2T MBB, even with a fixed warm dust component, is optimal for fitting the peak of the SED and determining  $T_c$ .

## APPENDIX B TEMPLATE LIBRARIES

We present the complete data sets that comprise each template in Figures 19, 20, and 21. The spectra are plotted as lines and the photometry as open circles. We use a different color for each source in a given subsample. We plot any available submillimeter data as the open squares. These data were not included in the fit, since they are not available for all sources, but they are plotted to illustrate how well the Rayleigh–Jeans tails of our templates agree with observations. The templates and associated uncertainties are plotted as the thick black lines and gray shaded regions. We also plot the warm modified blackbody and cold modified blackbody from Equation (2) as the long dashed and dotted lines, respectively. We remind the reader that the three libraries are not independent as they all contain the same sources divided according to different criteria.

## REFERENCES

- Alexander, D. M., Bauer, F. E., Brandt, W. N., et al. 2003, *AJ*, 126, 539  
 Alexander, D. M., Chary, R.-R., Pope, A., et al. 2008, *ApJ*, 687, 835  
 Armus, L., Charmandaris, V., Bernard-Salas, J., et al. 2007, *ApJ*, 656, 148  
 Armus, L., Charmandaris, V., Spoon, H. W. W., et al. 2004, *ApJS*, 154, 178  
 Armus, L., Mazzarella, J. M., Evans, A. S., et al. 2009, *PASP*, 121, 559  
 Barger, A. J., Cowie, L. L., & Wang, W.-H. 2008, *ApJ*, 689, 687  
 Battisti, A. J., Calzetti, D., Johnson, B. D., & Elbaz, D. 2015, *ApJ*, 800, 143  
 Bauer, F. E., Yan, L., Sajina, A., & Alexander, D. M. 2010, *ApJ*, 710, 212  
 Béthermin, M., Daddi, E., Magdis, G., et al. 2015, *A&A*, 573, 113  
 Béthermin, M., Dole, H., Beelen, A., & Aussel, H. 2010, *A&A*, 512, 78  
 Bournaud, F., Dekel, A., Teyssier, R., et al. 2011, *ApJL*, 741, L33  
 Brandl, B. R., Bernard-Salas, J., Spoon, H. W. W., et al. 2006, *ApJ*, 653, 1129  
 Brightman, M., Nandra, K., Salvato, M., et al. 2014, *MNRAS*, 443, 1999  
 Carilli, C. L., Daddi, E., Riechers, D., et al. 2010, *ApJ*, 714, 1407  
 Casey, C. M. 2012, *MNRAS*, 425, 3094  
 Casey, C. M., Berta, S., Béthermin, M., et al. 2012, *ApJ*, 761, 140  
 Chary, R. R., & Elbaz, D. 2001, *ApJ*, 556, 562  
 Choi, P. I., Yan, L., Im, M., et al. 2006, *ApJ*, 637, 227  
 Clemens, M. S., Negrello, M., De Zotti, G., et al. 2013, *MNRAS*, 433, 695  
 Coppin, K., Pope, A., Menéndez-Delmestre, K., et al. 2010, *ApJ*, 713, 503  
 da Cunha, E., Groves, B., Walter, F., et al. 2013, *ApJ*, 766, 13  
 Daddi, E., Elbaz, D., Walter, F., et al. 2010, *ApJL*, 714, L118  
 Dale, D. A., Aniano, G., Engelbracht, C. W., et al. 2012, *ApJ*, 745, 95  
 Dasyra, K. M., Yan, L., Helou, G., et al. 2009, *ApJ*, 701, 1123  
 Díaz-Santos, T., Charmandaris, V., Armus, L., et al. 2011, *ApJ*, 741, 32  
 Donley, J. L., Koekemoer, A. M., Brusa, M., et al. 2012, *ApJ*, 748, 142  
 Donley, J. L., Rieke, G. H., Alexander, D. M., et al. 2010, *ApJ*, 719, 1393  
 Downes, D., & Solomon, P. M. 1998, *ApJ*, 507, 615  
 Draine, B. T. 2003, *ARA&A*, 41, 241  
 Dunne, L., & Eales, S. A. 2001, *MNRAS*, 327, 697  
 Elbaz, D., Dickinson, M., Hwang, H. S., et al. 2011, *A&A*, 533, 119  
 Fadda, D., Yan, L., Lagache, G., et al. 2010, *ApJ*, 719, 425  
 Genzel, R., Tacconi, L. J., Graciá-Carpio, J., et al. 2010, *MNRAS*, 407, 2091  
 Hayward, C. C., Kereš, D., Jonsson, P., et al. 2011, *ApJ*, 743, 159  
 Hernán-Caballero, A., Alonso-Herrero, A., Hatziminaoglou, E., et al. 2015, *ApJ*, 803, 109  
 Hickox, R. C., & Markevitch, M. 2007, *ApJ*, 671, 1523  
 Hwang, H.-S., Elbaz, D., Dickinson, M., et al. 2011, *A&A*, 535, 60  
 Jonsson, P. 2006, *MNRAS*, 372, 2  
 Kartaltepe, J. S., Dickinson, M., Alexander, D. M., et al. 2012, *ApJ*, 757, 23  
 Kartaltepe, J. S., Sanders, D. B., Silverman, J. D., et al. 2015, *ApJ*, 806, 35  
 Kennicutt, R. C., Jr. 1998, *ApJ*, 498, 541  
 Kirkpatrick, A., Calzetti, D., Kennicutt, R., et al. 2014a, *ApJ*, 789, 130  
 Kirkpatrick, A., Pope, A., Alexander, D. M., et al. 2012, *ApJ*, 759, 139  
 Kirkpatrick, A., Pope, A., Aretxaga, I., et al. 2014b, *ApJ*, 796, 135  
 Kirkpatrick, A., Pope, A., Charmandaris, V., et al. 2013, *ApJ*, 763, 123  
 Kocevski, D. D., Faber, S. M., Mozena, M., et al. 2012, *ApJ*, 744, 148  
 Lacy, M., Sajina, A., Petric, A. O., et al. 2007, *ApJL*, 669, L61  
 Lacy, M., Storrie-Lombardi, L. J., Sajina, A., et al. 2004, *ApJS*, 154, 166  
 Lanz, L., Hayward, C. C., Zezas, A., et al. 2014, *ApJ*, 785, 39  
 Lee, N., Sanders, D. B., Casey, C. M., et al. 2013, *ApJ*, 778, 131  
 Lin, L., Dickinson, M., Hung-Yu, J., et al. 2012, *ApJ*, 756, 71  
 Luo, B., Bauer, F. E., Brandt, W. N., et al. 2008, *ApJS*, 179, 19  
 Lutz, D., Yan, L., Armus, L., et al. 2005, *ApJL*, 632, L13  
 Madau, P., & Dickinson, M. 2014, *ARA&A*, 52, 415  
 Magdis, G., Daddi, E., Béthermin, M., et al. 2012, *ApJ*, 760, 6  
 Magnelli, B., Elbaz, D., Chary, R. R., et al. 2011, *A&A*, 528, A35  
 Magnelli, G., Saintonge, A., Lutz, D., et al. 2012, *A&A*, 548, 22  
 Martínez-Sansigre, A., Karim, A., Schinnerer, E., et al. 2009, *ApJ*, 706, 184  
 Martínez-Sansigre, A., Lacy, M., Sajina, A., & Rawlings, S. 2008, *ApJ*, 674, 676  
 Menéndez-Delmestre, K., Blain, A. W., Smail, I., et al. 2009, *ApJ*, 699, 667  
 Mullaney, J. R., Alexander, D. M., Goulding, A. D., & Hickox, R. C. 2011, *MNRAS*, 414, 1082  
 Mullaney, J. R., Daddi, E., Béthermin, M., et al. 2012, *ApJL*, 753, L30  
 Murphy, E. J., Chary, R.-R., Alexander, D. M., et al. 2009, *ApJ*, 698, 1380  
 Murphy, E. J., Chary, R.-R., Dickinson, M., et al. 2011, *ApJ*, 732, 126  
 Nelson, E., van Dokkum, P., Franx, M., et al. 2014, *Natur*, 513, 394  
 Noeske, K. G., Weiner, B. J., Faber, S. M., et al. 2007, *ApJL*, 660, L43  
 Nordon, R., Lutz, D., Schweitzer, M., et al. 2010, *A&A*, 518, L24  
 O'Dowd, M. J., Schiminovich, D., Johnson, B. D., et al. 2011, *ApJ*, 741, 79  
 Peeters, E., Spoon, H. W. W., & Tielens, A. G. G. M. 2004, *ApJ*, 613, 986  
 Penner, K., Pope, A., Chapin, E. L., et al. 2011, *MNRAS*, 410, 2749  
 Petric, A. O., Armus, L., Howell, J., et al. 2011, *ApJ*, 730, 28  
 Planck Collaboration 2011, *A&A*, 536, A25  
 Polletta, M., Omont, A., Berta, S., et al. 2008, *A&A*, 492, 81  
 Pope, A., Scott, D., Dickinson, M., et al. 2006, *MNRAS*, 370, 1185  
 Pope, A., Wagg, J., Frayer, D., et al. 2013, *ApJ*, 772, 92  
 Pope, A., Chary, R. R., Alexander, D. M., et al. 2008, *ApJ*, 675, 1171  
 Popesso, P., Dickinson, M., Nonino, M., et al. 2009, *A&A*, 494, 443  
 Retzlaff, J., Rosati, P., Dickinson, M., et al. 2010, *A&A*, 511, A50  
 Riechers, D. A., Pope, A., Daddi, E., et al. 2014, *ApJ*, 786, 31  
 Sajina, A., Yan, L., Armus, L., et al. 2007, *ApJ*, 664, 713  
 Sajina, A., Yan, L., Lutz, D., et al. 2008, *ApJ*, 683, 659  
 Sajina, A., Yan, L., Fadda, D., Dasyra, K., & Huynh, M. 2012, *ApJ*, 757, 13

- Sanders, D. B., & Mirabel, I. F. 1996, [ARA&A](#), **34**, 749
- Scoville, N., Aussel, H., Sheth, K., et al. 2014, [ApJ](#), **783**, 84
- Siebenmorgen, R., Heymann, F., & Efstathiou, A. 2015, [A&A](#), in press (arXiv:[1508.04343](#))
- Snyder, G. F., Hayward, C. C., Sajina, A., et al. 2013, [ApJ](#), **768**, 168
- Solomon, P. M., & Vanden Bout, P. A. 2005, [ARA&A](#), **43**, 677
- Springel, V. 2005, [MNRAS](#), **364**, 1105
- Springel, V., Yoshida, N., & White, S. D. M. 2001, [NewA](#), **6**, 51
- Stanley, F., Harrison, C. M., Alexander, D. M., et al. 2015, [MNRAS](#), **453**, 591
- Stern, D., Assef, R. J., Benford, D. J., et al. 2012, [ApJ](#), **753**, 30
- Stern, D., Eisenhardt, P., Gorjian, V., et al. 2005, [ApJ](#), **631**, 163
- Stierwalt, S., Armus, L., Charmandaris, V., et al. 2014, [ApJ](#), **790**, 124
- Stierwalt, S., Armus, L., Surace, J. A., et al. 2013, [ApJS](#), **206**, 1
- Sturm, E., Hasinger, G., Lehmann, I., et al. 2006, [ApJ](#), **642**, 81
- Szokoly, G. P., Bergeron, J., Hasinger, G., et al. 2004, [ApJS](#), **155**, 271
- Teplitz, H. I., Desai, V., Armus, L., et al. 2007, [ApJ](#), **659**, 941
- Treister, E., Urry, M., Schawinski, K., et al. 2010, [ApJL](#), **722**, L238
- Veilleux, S., Rupke, D. S. N., Kim, D.-C., et al. 2009, [ApJS](#), **182**, 628
- Wang, W.-H., Cowie, L. L., Barger, A. J., Keenan, R. C., & Ting, H. C. 2010, [ApJS](#), **187**, 251
- Weedman, D. W., Le Floch, E., Higdon, S. J. U., et al. 2006, [ApJ](#), **638**, 613
- Weiß, A., Kovács, A., Coppin, K., et al. 2009, [ApJ](#), **707**, 1201
- Wu, Y., Charmandaris, V., Hao, L., et al. 2006, [ApJ](#), **639**, 157
- Xue, Y. Q., Luo, B., Brandt, W. N., et al. 2011, [ApJS](#), **195**, 10
- Yan, L., Sajina, A., Fadda, D., et al. 2007, [ApJ](#), **658**, 778
- Zamojski, M., Yan, L., Dasyra, K., et al. 2011, [ApJ](#), **730**, 125